

Growth of Graphene by Silicon Carbide Sublimation

Tanaka Benton

Applied Mathematics and Pre-Engineering, Atlanta Metropolitan State College

NNIN REU Site: Howard Nanoscale Science and Engineering Facility, Howard University, Washington, DC

NNIN REU Principal Investigator: Dr. Gary Harris, Department of Electrical and Computer Engineering, Howard University

NNIN REU Mentor: Mr. Crawford Taylor, Department of Electrical and Computer Engineering, Howard University

Contact: benton1tanaka@gmail.com, gharris1124@gmail.com, c_taylor@howard.edu

Abstract:

Graphene has become the material of choice for several investigators because of its desirable properties. This two-dimensional “super” material is hexagonally bonded in an sp^2 carbon arrangement. Successful methods for growing graphene include chemical vapor deposition (CVD) on metal surfaces like copper or nickel and by sublimation of silicon carbide (SiC). Graphene on SiC is of particular interest because it does not require transfer onto another substrate like graphene grown on copper does and the process is not as strenuous and damage-prone. This work investigates the conditions necessary for producing graphene on C-terminated 6H-SiC wafers by sublimation. Hydrogen (H_2) surface etching was performed at 1200°C, while sublimation was done between 1500°C-1700°C in the presence of argon (Ar) gas, at a pressure of 200 Torr. The growth times were varied from 15-60 minutes. Scanning electron microscopy (SEM) and Raman spectroscopy were used to characterize the results obtained for single and multilayer graphene.

Introduction:

Graphene, due to its specific aggregation of carbon atoms, forms a two-dimensional honeycomb crystal lattice. Graphene’s first experimental discovery, via micromechanical cleavage using Scotch tape, catalyzed many researchers’ interest. Since its discovery, unforeseen conclusions regarding the immense strength, thinness and durability of the material have spun into copious research topics within engineering and science. Since graphene’s first experimental discovery, many techniques have been explored to increase its reproducibility. Core problems remain in regards to growing defect-free large area graphene.

Experimentation was designed to determine growth parameters for producing single, bi-layer and/or multi-layer graphene with large grain boundaries. Therefore, we chose to investigate the formation of graphene by sublimation of SiC substrates using a high temperature CVD system.

Experimental Procedure:

In this work, 4H and 6H SiC substrates were cut into smaller 1 × 1 cm pieces, which were then cleaned by acetone and methanol sonication, followed by a hydrofluoric acid dip. The samples were then loaded into the CVD system, where they were purged with H_2 for two cycles of five minutes at 200 Torr. The temperature was then increased from room temperature to the etch temperature

of 1200°C in H_2 , after which the temperature was again increased to the sublimation temperature of 1500 -1700°C in Ar. C-terminated 6H-SiC substrates were etched for 30 minutes at 1200°C in H_2 and sublimed for 30 minutes at 1700°C in Ar. Conversely, Si-terminated 6H-SiC substrates were etched for 60 minutes in H_2 at 1200°C and sublimed at 1500°C for 60 minutes in Ar. At the end of the growth cycle, the temperature was decreased to room temperature with the system being purged with Ar before removing the samples.

Results:

We concentrated on graphene by sublimation of 6H-SiC substrates relative to the other polytypes. Originally, it was observed that H_2 etch times contributed greatly to how efficiently silicon would sublime. Etch times ranged from 15-120 minutes and SEM was used to obtain surface imaging. There was expectancy for the surface to be smooth and consistent, but etch times longer than 60 minutes showed pits and scratches; depicting over-etching or high penetration. With this discovery, further etches were done for 30-60 minutes instead.

The sublimation growths under argon were then conducted, firstly at 1500°C and later increased to 1700°C. Increasing the growth temperature to 1700°C was the pinnacle modification for C-terminated samples.

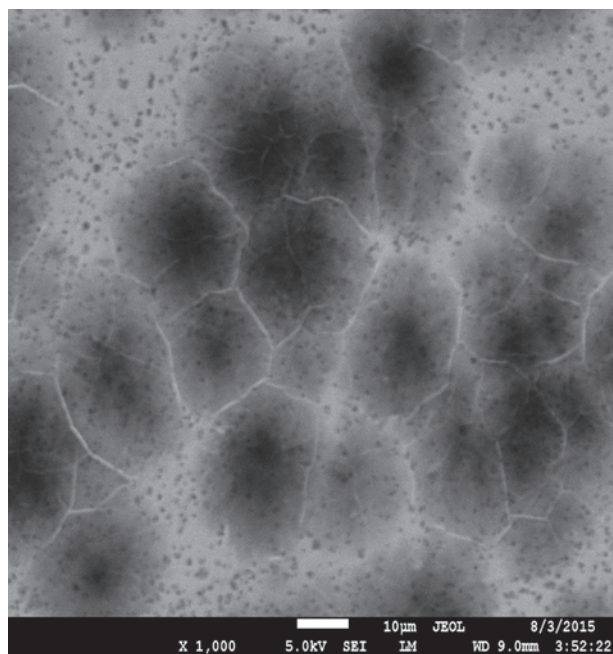
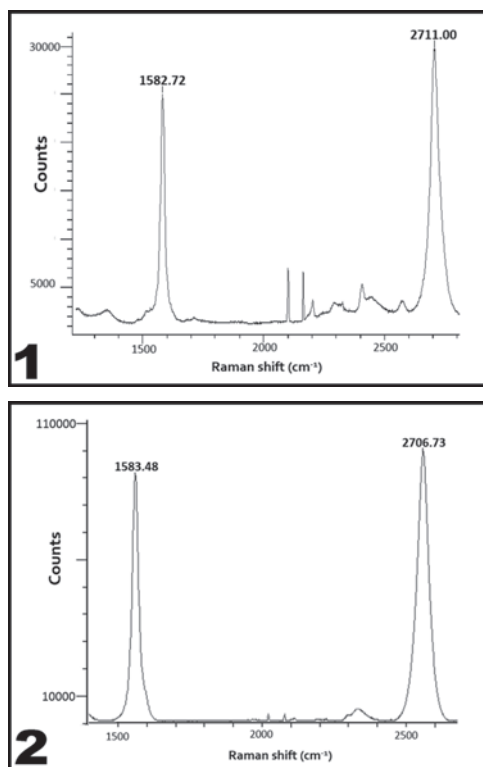


Figure 1, top left: Raman spectroscopy results of graphene on C-terminated 6H-SiC. **Figure 2, bottom left:** Raman spectroscopy results of graphene on Si-terminated 6H-SiC. **Figure 3, above:** SEM image of C-terminated 6H-SiC.

Using Raman spectroscopy, we characterized a G-band of 1587.82 cm⁻¹ and 2D-band of 2711.00 cm⁻¹ with a 2:1 ratio between the bands (Figure 1). Additionally, Si-terminated samples showed progress in growth when etch and growth times were increased to 60 minutes. Here the temperature remained at 1500°C with a G-band of 1583.48 cm⁻¹ and 2D-band of 2706.73 cm⁻¹ with a 3:1 ratio between bands (Figure 2).

Conclusions:

Small deviations in growth parameters caused significant variations in results. After numerous adjustments to the growth parameters and studying each result, patterns of epitaxial graphene growth arose for very specific conditions; noticeable for both the Si-terminated and C-terminated 6H-SiC substrates. Characterization by Raman spectroscopy, indicated bi-layer and multi-layer graphene growth by SiC sublimation. Si-terminated 6H-SiC grain sizes were 5.0-7.5 µm. In comparison, C-terminated 6H-SiC grain sizes were three times larger than those on Si-terminated, measuring 20-31 µm (Figure 3).

Future Work:

We intend to investigate the cause of grain boundary size deviations in C-terminated and Si-terminated 6H-SiC substrates. Also, we hope to further understand the parameter augmentations that affect graphene growth.

Lastly, growth of graphene by sublimation on 3C-SiC grown on silicon may be useful in understanding and achieving high quality graphene growths.

Acknowledgements:

I would like to acknowledge the National Science Foundation (Grant No. ECCS-0335765) and the National Nanotechnology Infrastructure Network Research Experience for Undergraduates (NNIN REU) Program for this immense opportunity in science. I would like to thank the Howard Nanoscale Science and Engineering Facility and its staff for selecting me to perform research within their laboratories and assisting me throughout this process. Lastly, I would like to acknowledge my advisors, mentors, and home institution, Atlanta Metropolitan State College, for advocacy in my many endeavors.

References:

- [1] Hodkiewicz, J; "The Importance of Tight Laser Power Control When Working with Carbon Nanomaterials"; Thermo Scientific Application Note ANS1948, 4 (2010).
- [2] de Heer, W; "Large Area and Structures Epitaxial Graphene Produced by Confinement Controlled Sublimation of Silicon Carbide"; PNAS, vol. 108, 6 (2011).
- [3] Murray, S.; "Graphene Growth Studies on Copper (111) and Silicon Carbide Substrates"; SUNY College of Nanoscale Science and Engineering, 2014. Web. 2014.
- [4] Dumé, Belle; "Graphene has record-breaking strength"; IOP Physics World, 17 Jul 2008. Web. 2008.

Electric Field-Directed Assembly of Nanowires on Patterned Electrodes

Nermina Brljak

Chemistry, Florida State University

NNIN REU Site: Penn State Nanofabrication Laboratory, The Pennsylvania State University, University Park, PA

NNIN REU Principal Investigator: Dr. Christine Keating, Chemistry, The Pennsylvania State University

NNIN REU Mentor: Sarah Boehm, Chemistry, The Pennsylvania State University

Contact: nb13e@my.fsu.edu, keating@chem.psu.edu, sjb340@psu.edu

Abstract:

Many researchers have shown that the assembly of nanowires could lead to future electronic and optical devices [1]. This project focused on assembly of gold nanowires in an alternating current (AC) electric field between parallel electrodes. Assembling nanowires requires a great deal of control, which is why the electric field system is ideal. The bottom electrode was lithographically fabricated and contained organized micro-patterned pillars made from photoresist on top of a layer of titanium and gold. The top electrode was an indium tin oxide (ITO)-coated glass coverslip. Since this electrode was transparent, the assembly could be monitored in real time. Pillars were 3 μm tall and 3-20 μm in diameter, with spacing varying from 10-55 μm . These pillars acted as nucleation sites for the assemblies. Electric field-induced dipoles aligned the nanowires parallel to the field lines between the two electrodes. By varying different parameters, such as voltage and frequency, specific and controlled placement of the nanowires was possible and could be varied in real time. The assemblies could be reversed and replicated by switching the field on and off. This technique is promising for generating nanowire assemblies for electronic applications.

Patterned Electrode:

The patterned substrate was photolithography fabricated to create photoresist posts with desired diameters and separation distances. Figure 1 shows the fabrication process. First, a layer of 10 nm of titanium (Ti) was deposited by electron beam evaporation onto a glass coverslip, followed by a 30 nm layer of gold (Au). A 3.2 μm layer of positive photoresist was then spin-coated onto the substrate. Using a stepper exposure tool, the area around the desired posts was exposed to high intensity UV light through a patterned mask. The sample was then developed in MF CD 26 to remove the exposed areas of the photoresist. Two designs were used; a hexagonal configuration and a square pattern.

Experimental Design:

As shown in Figure 2, voltage was applied through the patterned Au electrode and a transparent ITO-coated glass coverslip. A spacer was placed in between the two electrodes. This spacer was completely filled with 2.75 μL diluted solution of nanowires in deionized water. The nanowires used were silica-coated gold nanowires that measured 2.5 μm in length and 300 nm in diameter. Frequency and voltage were slowly increased over time to monitor the different assemblies at various conditions.

Results:

Prior to electric field application, the nanowires diffused in solution, lying down above the bottom electrode. Once the field was applied,

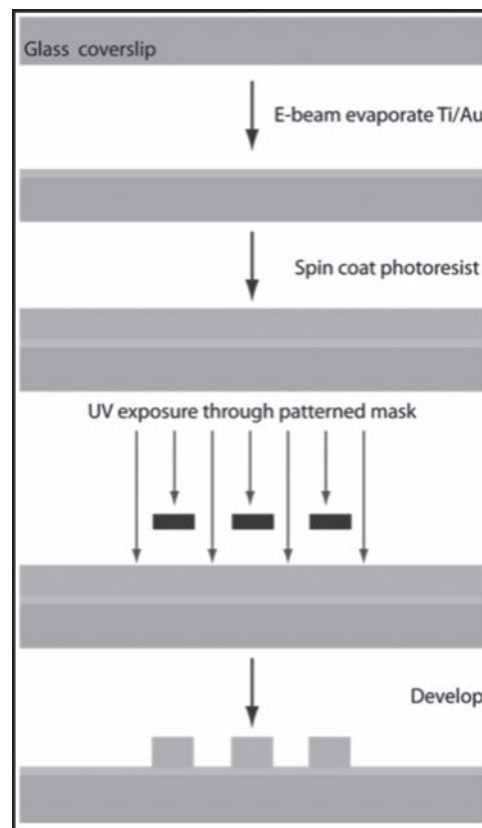


Figure 1: Photolithography fabrication process for patterning photoresist posts atop a gold-coated glass coverslip.

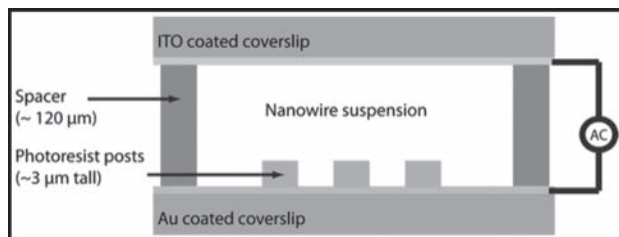


Figure 2: Side view of experimental set-up. Electric field is applied vertically, across the top and bottom electrodes through the nanowire solution.

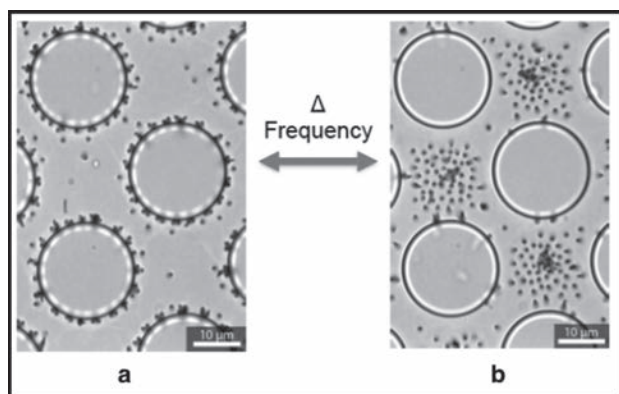


Figure 3: Optical microscope images taken from the bottom of the assembly using transmitted light. The large grey circles are the photoresist posts and the small black dots are the standing nanowires. This shows the different assemblies at two field conditions, (a) 330 V/cm, 400 kHz, and (b) 330 V/cm, 25 kHz.

the nanowires stood between the two electrodes, parallel to the electric field lines (Figure 3a). As the frequency increased, the dielectrophoretic (DEP) force increased. DEP occurred when the electric field caused the nanowires to obtain a field-induced dipole causing them to stand [2]. The local electric field strength around the fabricated posts was intensified, which caused the nanowires to nucleate around them. The posts with a smaller diameter required a higher field strength to nucleate these nanowires than the posts with larger diameters. As the frequency decreased, the electrohydrodynamic flow within the solution increased. This flow caused the nanowires to assemble in the stagnation areas between the posts (Figure 3b).

These assemblies could be reversibly formed and disassembled. When the field conditions were turned off, the nanowires separated from one another and diffused (Figure 4b). When the electric field was turned back on, the nanowires stood parallel to the field lines once again (Figure 4c). The nanowires reassembled not into the same exact positions as before but into similar organizations. However, the time it took for the nanowires to change orientation varied

depending on the field conditions. This allowed for the assemblies to be reversible. When the field conditions were turned off, the number of visible nanowires increased. When the field was on, what appeared to be two nanowires (circled in Figure 4a), ended up being three nanowires when the field was turned off (circled in Figure 4b). Since the assemblies were being viewed from the bottom, the extra nanowires were not visible.

It can be hypothesized that since the nanowires had a field-induced dipole-dipole interaction, chaining in the z-direction occurred [3]. Figure 4d shows the possible chaining in the z-direction of a pair of nanowires. This kind of cluster trend occurred within every pattern organization and was not affected by the field conditions.

Conclusions and Future Work:

Overall, using a photoresist-patterned electrode successfully served as nucleation sites for nanowires to assemble around. By tuning the electric field conditions, different assemblies could be created. The AC electric field is ideal for assembling these nanowires because it enables control and tunability in real time.

Acknowledgements:

I would like to thank my mentor, Sarah Boehm, for all of her help and guidance. I would also like to thank the Keating group and especially my principal investigator, Dr. Christine Keating. Another thank you to the Materials Research Institute at Pennsylvania State University, the National Nanotechnology Infrastructure Network Research Experience for Undergraduates Program and NSF funding under Grant No. ECCS-0335765.

References:

- [1] Grzelczak, M.; Vermant, J.; Furst, E. M.; Liz-Marzán, L. M. *ACS Nano*, 2010 4(7), 3591-3605.
- [2] Smith, B. D.; Mayer, T.S.; Keating, C. D.; *Annu. Rev. Phys. Chem.* 2012, 241-263.
- [3] Boehm, S. J.; Lin, L.; Betancourt, K. G.; Emery, R.; Mayer, J. S.; Mayer, T.S.; Keating, C. D.; *Langmuir*, 2015, 31(21), 5779-5786.

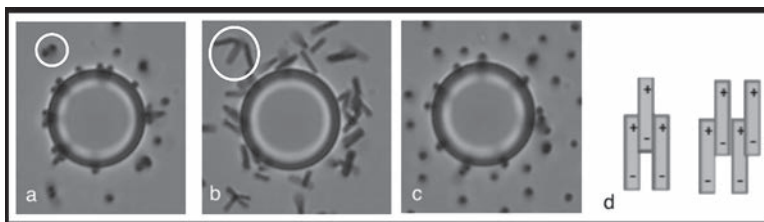


Figure 4: Images of when the field conditions are turned on (a), turned off (b) and turned back on (c). Possible chaining of pairs (d).

Zinc Oxide Deposition Methods for Opto-Electronic Applications

Benjamin Carberry

Electrical Engineering, University of Florida

NNIN REU Site: UCSB Nanofabrication Facility, University of California, Santa Barbara, CA

NNIN REU Principal Investigator: Dr. Steven DenBaars, Materials Department and Department of Electrical and Computer Engineering, UCSB

NNIN REU Mentor: Asad Mughal, Materials Department, University of California, Santa Barbara

Contact: bcarberry93@aol.com, denbaars@engineering.ucsb.edu, asad_mughal@umail.ucsb.edu

Abstract:

The purpose of this study is to investigate the feasibility of combining the atomic layer deposition (ALD) and hydrothermal deposition methods for growing zinc oxide (ZnO) thin films for opto-electronic applications. The main application considered throughout this study is the transparent conductive oxide (TCO) layer in gallium nitride (GaN) LEDs. The focus of this research was to maximize the optical transparency and minimize electrical resistivity of the grown ZnO films. A resistivity value as low as 2.75 milli-ohm centimeters ($\text{m}\Omega\cdot\text{cm}$) was obtained for ZnO, which is comparable to the measured resistivity of ITO, $1.09 \text{ m}\Omega\cdot\text{cm}$. Optical transmission measurements showed that a ZnO film with a thickness of 1.34 micrometer (μm) stays within around 10% of an ITO film with a thickness of $0.33 \mu\text{m}$. Despite already yielding values comparable with ITO, the ZnO film performance can probably still improve since further optimizations can be made to the hydrothermal deposition process.

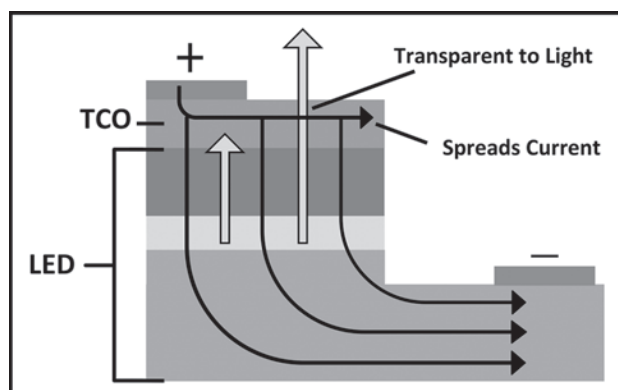
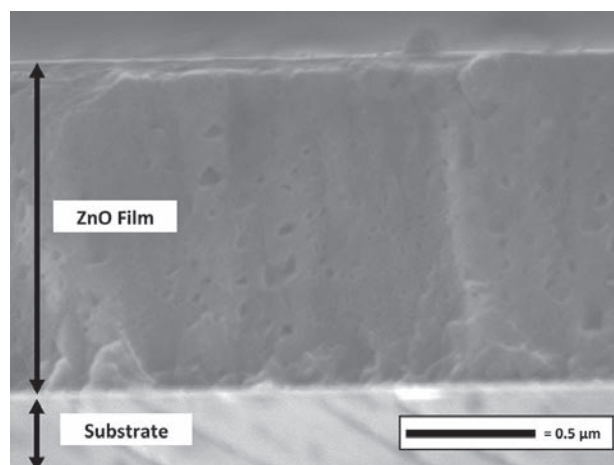


Figure 1, above: Basic diagram of LED with TCO layer.

Figure 2, right: SEM image of ZnO film.



Introduction:

Due to its relatively low cost, ZnO is receiving attention as a viable alternative to the current industry standard, indium tin oxide (ITO), for use as the TCO material [1]. The TCO layer is an essential component of opto-electronic devices because of its ability to spread current while also being transparent to light. Figure 1 shows a basic diagram of the TCO layer on an LED.

Numerous methods exist for depositing a thin film of ZnO onto a substrate, but several of these methods require expensive machinery and very controlled environments. Hydrothermal deposition, however, is a relatively simple method because it does not have these requirements [2]. The only prerequisite is a thin seed layer on which to grow

the hydrothermal film, which is precisely grown using ALD. The main goal of the research this summer was to observe the electrical and optical performance of the ZnO films grown specifically using ALD and hydrothermal deposition. Figure 2 shows a scanning electron microscope (SEM) image of the ZnO thin film.

Process:

ZnO thin films were deposited on Al_2O_3 (sapphire) substrates in four steps: 1) ALD seed layer, 2) anneal treatment, 3) hydrothermal layer, and 4) final anneal treatment.

In the ALD seed layer step, diethylzinc was used as the zinc precursor, or source, and we found that using H_2O as the oxygen precursor, while running the process at $300^\circ C$, gave the highest quality seed layer structure with the highest conductivity. The standard number of cycles was chosen to be 25, which yielded a thickness of around 4 nanometers (nm). The self-limiting nature of ALD means that each cycle produces only single layers of a certain thickness; this makes ALD an excellent method for growing the seed layer.

The annealing (heat treatment) step had the best results when done at $700^\circ C$ for 30 minutes in the presence of nitrogen gas. The hydrothermal deposition process was carried out in an aqueous solution heated to and held at $90^\circ C$ for two hours. The standard solution used consisted of 1.3 milli-liters (mL) of NH_4OH , 25mL of 5 millimolar (mM) $ZnNO_3$ and 5 mM of Na-Citrate. To help increase conductivity, the solution was also doped with aluminum (Al), gallium (Ga), and indium (In) before the hydrothermal process began. The amounts of dopants used ranged from 0.1 mM to 4 mM.

The main mechanism behind hydrothermal deposition is that as the temperature and pH level increases, the solubility of the aqueous solution decreases, and ZnO becomes more likely to form. First, the ionized zinc and

hydroxide particles will form zinc hydroxide, and then the zinc hydroxide will dehydrate into zinc oxide and water.

Data:

Some of the best results recorded are shown in Figures 3 and 4. Figure 3 shows the different resistivity values of doped and undoped ZnO films compared to the measured resistivity of ITO. While ITO has the lowest resistivity at $1.089\ m\Omega\cdot cm$, one of the best results obtained for ZnO was with a 0.4 mM Ga-doped film. Other dopants and amounts seemed to increase the resistivity relative to the undoped ZnO film, which had a resistivity of $3.86\ m\Omega\cdot cm$.

Figure 4 shows the difference in transmission between a sapphire substrate without a film, ITO, and doped ZnO. Without any film, the substrate transmits around 85%. With a 0.33 micrometer (μm) thick ITO film, the transmission ranges between 68-86% in the visible spectrum. Despite being thicker, the $1.33\ \mu m$ film of ZnO remains within 10% of the ITO film throughout most of the visible spectrum.

Conclusions:

This research confirmed that using the combination of ALD and hydrothermal deposition is a feasible method for growing ZnO, yielding optical and electrical performance comparable to the industry standard, ITO. However, there is still room for improvement. The hydrothermal deposition method needs to be investigated further to obtain a film with more transparency and a more controlled thickness. In addition, attenuation coefficients need to be obtained so optical performance can be accurately quantified independently of film thicknesses. Finally, LEDs need to be processed to assess the actual light quality and efficiency.

Acknowledgements:

I would like to thank the NNIN REU Program for providing me with an opportunity to participate in nanotechnology research, and I thank my mentor, Asad Mughal, for introducing me to graduate and materials science research. I would also like to thank my principal investigator, Dr. Steven DenBaars, and my site coordinator, Wendy Ibsen. The National Science Foundation supported this research under Grant No. ECCS-0335765.

References:

- [1] Ellmer, K. (2012). Past achievements and future challenges in the development of optically transparent electrodes. *Nature Photonics*, 6(12), 809–817. <http://doi.org/10.1038/nphoton.2012.282>.
- [2] Kim, J. H., Andeen, D., and Lange, F. F. (2006). Hydrothermal growth of periodic, single-crystal ZnO microrods and microtunnels. *Advanced Materials*, 18(18), 2453–2457. <http://doi.org/10.1002/adma.200600257>.

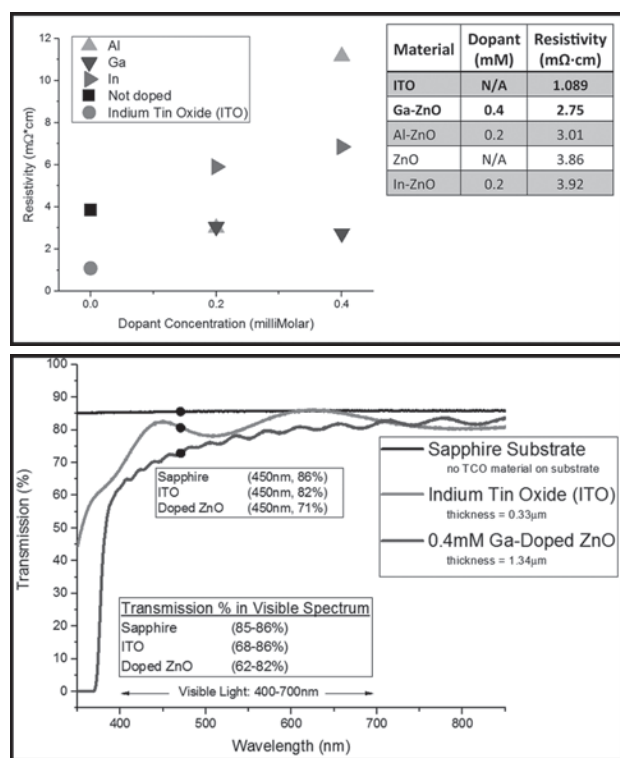


Figure 3, top: Left; Resistivity values vs. Dopant Concentration (lower resistivity means higher conductivity). Right; Table of lowest resistivity values for comparison.

Figure 4, bottom: Optical Transmission vs. Wavelength for the sapphire substrate alone, ITO, and doped ZnO.

Mechanical Testing of OPVs using Flextrode: An ITO-Free, Transparent, Polymer-Based Electrode

Isaac DiGennaro

Chemistry, Missouri University of Science and Technology

NNIN REU Site: Stanford Nanofabrication Facility, Stanford University, Stanford, CA

NNIN REU Principal Investigator: Professor Reinhold H. Dauskardt, Materials Science and Engineering, Stanford University

NNIN REU Mentor: Nick Rolston, Applied Physics, Stanford University

Contact: isdwxc@mst.edu dauskardt@stanford.edu rolston@stanford.edu

Abstract:

Organic photovoltaic (OPV) cells may offer a means to rapidly produce low-cost devices by printing thin films onto plastic substrates in ambient conditions. Indium-tin oxide (ITO) is the standard electrode for OPVs, but is brittle, prohibitively expensive, and not scalable. Flextrode, a transparent, flexible electrode composed of conductive polymers, was recently developed as a move towards cheaper materials with better mechanical properties than ITO. This project investigated effects of mechanical strain on the cohesion and function of the flextrode layer as part of an OPV. Films on a plastic substrate were deformed to varied strains, while monitoring film behavior with an optical microscope. Changes in surface morphology were characterized with optical and atomic force microscopy to determine the strain tolerance of the films. Additionally, *in situ* measurements of conductivity and photovoltage during tensile tests determined the effect of strain on the functionality of the layers. Flextrode proved to be a mechanically robust alternative to ITO that resists cracking up to a 25% strain with minimal loss of conductivity.

Introduction:

Organic photovoltaics is a recently developed field that uses polymers in electron donor-acceptor pairs to harness the photoelectric effect. OPVs offer solutions to a number of the limitations of silicon cells. For instance, they may be mass-produced at much lower cost due to cheap starting materials and simple fabrication processes. In addition, the light weight and flexibility is compatible with easy transport and deployment, and wearable electronics applications. However, OPV research still faces a number of hurdles in reliability and power conversion efficiency (PCE). OPV efficiency lags behind that of traditional cells, and they degrade due to environmental stressors, further lowering PCE. In addition, the cells must withstand stresses from deformation of the plastic substrate. Heretofore, adhesive and cohesive strength of OPVs has been low, causing mechanical failure. Flextrode, a polymer based, printed electrode, was developed as an alternative to ITO, which is brittle and plagued by many of the limitations of silicon cells. Prior work has characterized its fabrication and electrical properties [1]; this project investigated the tensile strain tolerance of a flextrode based OPV and the films that comprise it.

Methods:

The films of interest are printed sequentially onto the plastic substrate: beginning with only flextrode and zinc oxide

electron transport layers (ETL), followed by active layer, then the conductive polymer hole transport layer (HTL), and finally the complete device. Samples were prepared with one, two, or three layers and each was incrementally strained by tensile loading. The resulting changes in surface morphology were characterized using optical and atomic force microscopy (AFM). Electrical measurements were also taken to determine the functionality of the cells under strain. The resistance of the flextrode layer and photocurrent generated by the full device were measured during tensile tests using a multimeter.

Results and Discussion:

Cohesive cracking due to strain was characterized with AFM in order to determine the robustness of the individual films. Table 1 shows the strain at which cracks were first detected (crack onset) and at which they propagated

Cell Layer	Crack onset (% Strain)	Cracks through (% Strain)
HTL (PEDOT:PSS)	No cracking	Delamination at 15 %
Active (P3HT:PCBM)	6	30
ETL (ZnO)	5	10
Flextrode (PEDOT:PSS)	25	30

Table 1: Strain tolerance of films.

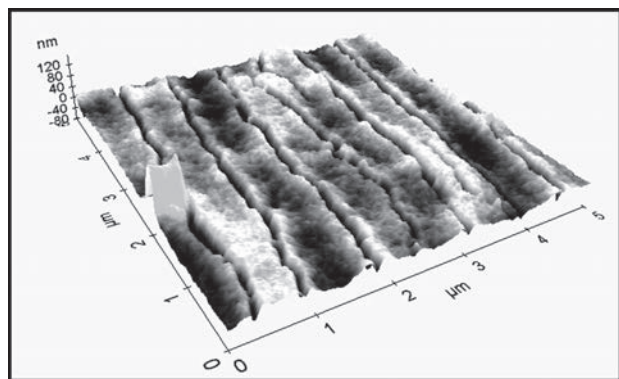


Figure 1: AFM image cracked ETL on flextrode at 20% strain (60-80 nm cracks).

through the film (cracks through). Delamination of the HTL due to poor adhesion to the underlying active layer was found to be the first cause of total device failure. Onset of surface cracking of the active layer occurred at 6% strain, but the devices continued to function despite this. Figure 1 shows surface cracking of the ETL on flextrode in a 5 μm square AFM topography image. Before straining, the surface was very smooth with 3-5 nm surface features; crack depth, width, and density increased with greater strain. Flextrode was shown to be mechanically robust to 25% strain. This is nearly an order of magnitude above the strain tolerance of ITO, which begins to crack at 3% strain [2].

The changes in surface morphology were correlated with the functionality of the films. Strain slightly decreased the conductivity of the flextrode layer, as shown in Figure 2, but it retained 75% of its function at 25% strain. The layer had not failed catastrophically even by 60% strain, a deformation that requires kilonewtons of force.

Next, function of the full devices under strain was tested by photocurrent measurements, the results of which are shown in Figure 3. Background effects interfered with quantitative measurements, but qualitative trends were apparent. At strains less than five percent (comparable to operating conditions), cracks reclose and function is restored upon relaxation. The full device retains functionality to 25% strain. Though crack onset in the active layer at 6% strain causes some decrease in output, the complete cell is able to withstand deformations well beyond those expected in service.

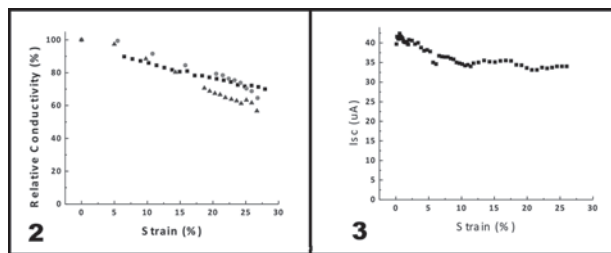


Figure 2, left: Conductivity measurements of flextrode during tensile testing. Figure 3, right: Photocurrent (I_{sc}) measured as a function of strain.

Conclusions:

Though OPVs face a number of challenges before they are market-ready, we have shown flextrode-based devices to be quite robust towards tensile strain. Surface morphology of the films was characterized with AFM to determine onset of cohesive cracking, and this was correlated with film functionality. Flextrode tolerated an order of magnitude higher strain than conventional ITO, retaining 75% of its original conductivity at 25% strain. Though the active layer begins to crack at 6% strain, actual device failure was caused by delamination of the HTL. Straining cells decreased their PCE, but the device continued to function at 25% strain, far beyond normal operating conditions. Flextrode is therefore shown to be a viable replacement for ITO, and more compatible with the fabrication process and applications of OPVs. Improvement of adhesion at the active layer-HTL interface will improve cells' mechanical durability, a critical step in realizing the potential of OPVs.

Acknowledgements:

Nick Rolston (mentor), Professor Reinhold Dauskardt (PI), Dr. Michael Deal (site coordinator), SNE, CIS, NNIN REU Program, NSF (ECCS-0335765).

References:

- [1] Frederik C. Krebs, 2009, 93, 4, 394-412.
- [2] Mora, et al. Electronic Materials Letters 2010, 10, 1033.

Infiltration, Imidization, and Cross-Linking of Polyimides in Molecular-Scale Confinement

Jade Fostvedt

Chemistry, University of South Dakota

NNIN REU Site: Stanford Nanofabrication Facility, Stanford University, Stanford, CA

NNIN REU Principal Investigator: Professor Reinhold H. Dauskardt, Materials Science and Engineering, Stanford University

NNIN REU Mentor: Scott G. Isaacson, Materials Science and Engineering, Stanford University

(2009 NNIN REU at Cornell; 2010 NNIN iREU at NIMS in Tsukuba, Japan)

Contact: jade.fostvedt@coyotes.usd.edu, rhd@stanford.edu, sgi@stanford.edu

Abstract:

Nanocomposite materials with a polymeric phase have novel properties—including exceptional toughness, strength, and low density—making them desirable for a variety of applications. Previous studies have shown that when the polymer within the nanocomposite material is confined to molecular-scale dimensions, polymer and nanocomposite properties are dramatically altered. In this work, we studied the effect of molecular-scale confinement on the synthesis and toughness of a nanocomposite material composed of polyimide in a nanoporous matrix. We optimized the properties of this composite material by varying the processing time and temperature. The extent of polymer infiltration, the ring-closing imidization reaction, and cross-linking of the polymer were studied. Finally, we measured the toughness of the composite material and found it to be increased by 87% as compared to the empty matrix. This work led to a better understanding of the effect of nanometer-scale confinement on the toughness of nanocomposite materials.

Introduction:

Composite materials combine dissimilar materials to produce improved properties, including low density and increased toughness and strength. One method of composite material synthesis involves infiltrating a polymer into the interconnected pore structure of a stiff inorganic matrix, which induces confinement of the polymer phase. In this work, we synthesized nanocomposite materials with polymers confined at molecular length-scales in order to test the limits of toughening with polymers in extreme confinement. The materials were created through a unique backfilling approach in which polymers are infiltrated into the pores of a nanoporous glass scaffold. This synthesis technique leads to uniform mixing of the two phases at small length-scales and produces uniform, high-quality films over large areas.

The confining matrix for this work was ethylene oxycarbosilane (Et-OCS), a porous organosilicate with a porosity volume of 47% and interconnected pores roughly 7 nm in diameter. Polyimide was chosen for the polymer phase in this work, as its ability to withstand high temperatures makes it ideal for future applications as a material for high-performance aerospace applications. Our objective for this work was to optimize the processing conditions for the Et-OCS/polyimide nanocomposite material and to test its mechanical properties.

Experimental:

The porous Et-OCS matrix was synthesized as a ~ 600 nm film on a silicon wafer and then cut into 1 × 1 cm² samples [1]. Each sample was then spin-coated with a thin film (~ 300 nm) of polyamic ethyl ester, a polyimide precursor manufactured by the U.S. Air Force. The sample was then cured under an inert atmosphere in a Yield Engineering Systems oven (Figure 1).

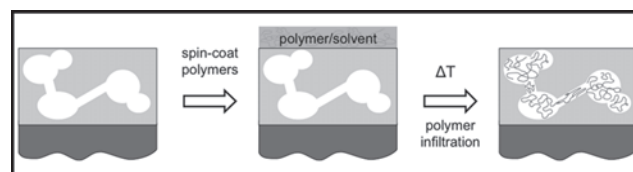


Figure 1: Infiltration strategy for Et-OCS/polyimide nanocomposite material.

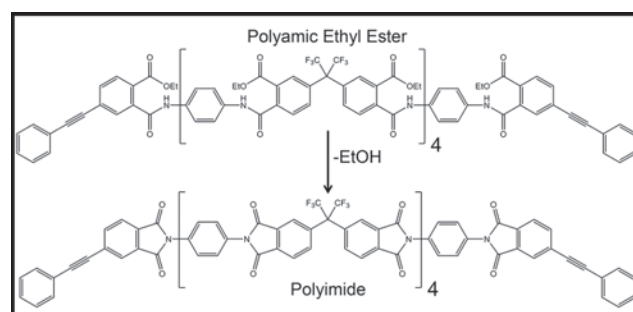


Figure 2: Imidization of polyamic ethyl ester to form polyimide.

During this high-temperature curing process, a number of changes can occur within the sample, all of which can affect the properties of the final product. First, the polymer infiltrates the pores of the matrix. Additionally, the polymer itself undergoes reactions in confinement: a ring can close in the polyamic ethyl ester structure, forming polyimide (Figure 2) and possible side products, and cross-linking can occur at the alkyne end-groups of the polymer chains. Infiltration of the polymer was monitored using depth profiling x-ray photoelectron spectroscopy (XPS). Chemical changes within the polymer structure were monitored using Fourier transform infrared spectroscopy (FTIR).

FTIR peaks for the various polymer species in the sample were then assigned and used to elucidate an imidization reaction mechanism for this process [2]. From the XPS and FTIR data, an ideal curing profile was selected to make nanocomposite samples with the maximum degree of infiltration, the largest amount of desired polyimide product, and the desired density of cross-linking. Finally, toughness of samples was assessed by making double cantilever beam (DCB) specimens containing the nanocomposite material of interest between two silicon beams (Figure 3). These specimens allowed us to measure the energy required to propagate a crack through the nanocomposite film, providing a quantitative measure of toughness.

Results and Discussion:

We found that imidization was most successful (gave the greatest ratio of desired product to side product) when the samples were cured at higher temperatures ($>300^{\circ}\text{C}$) for one hour. We also observed that infiltration was most complete when the samples were cured at a lower

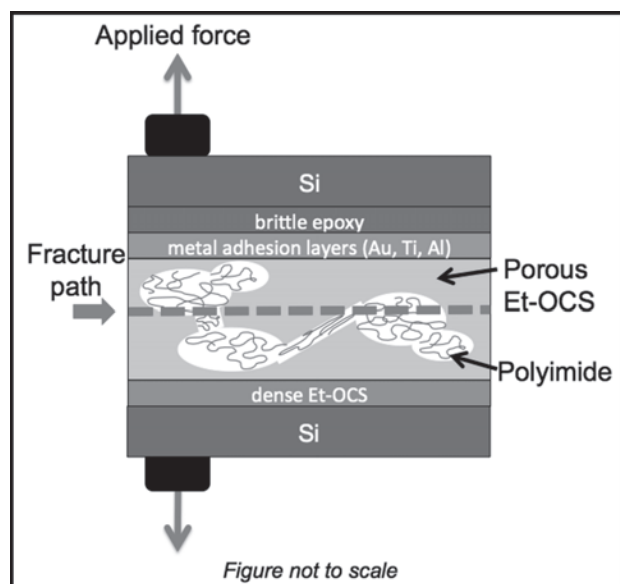


Figure 3: A schematic of a double cantilever beam specimen.

temperature ($<200^{\circ}\text{C}$) for four hours. Cross-linking did not occur until the cure temperature reached 360°C .

In order to synthesize a sample with optimized degrees of imidization, infiltration, and cross-linking, we chose a cure profile of 170°C for four hours to allow the polymer to infiltrate the pores and begin imidizing, followed by an hour-long period of increased temperature (370°C) in order to complete imidization and cross-link the confined polymer chains. Then, we measured the fracture energy of two nanocomposite films: one consisting of an Et-OCS matrix containing no polymer in the pores, and one containing polyimide processed according to the optimized curing conditions described above.

The sample with no polyimide in the pores had a cohesive fracture energy of 2.3 J/m^2 , a low toughness that is common for nanoporous glasses. The sample with cross-linked polyimide in the pores exhibited increased cohesive fracture energy of 4.3 J/m^2 , an 87% increase

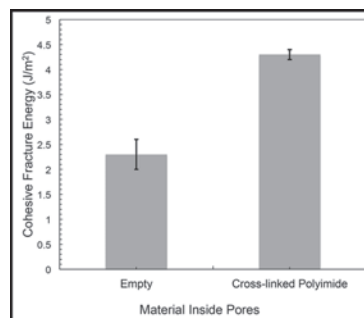


Figure 4: Cohesive fracture energy, a measure of toughness, increases when the pores of a nanoporous glass are filled with cross-linked polyimide.

in toughness compared to the unfilled film (Figure 4). Therefore, the objective of this project was met: we synthesized a novel nanocomposite material, tested its mechanical properties, and found it to be tougher than the empty matrix.

Future Work:

Future work will focus on further mechanical testing of samples containing polyimide with various degrees of cross-linking, investigating thermal stability of the nanocomposite material, and investigating other polyimides for filling the pores of the Et-OCS matrix.

Acknowledgements:

Thanks to Professor Reinhold Dauskardt, Scott Isaacson, Dr. Michael Deal, the Stanford Nanofabrication Facility, the NNIN REU Program, and IBM for their contributions. This work was supported by the Air Force Office of Science Research Grant No. FA9550-12-0120 and by the National Science Foundation Grant No. ECCS-0335765.

References:

- [1] Frot, T., et al. *Adv. Mater.* 23, 2828-2831 (2011).
- [2] Brekner, M.J., et al. *J. Polym. Sci.* 25, 2479-2490 (1987).

Ultrathin, Smooth, and Stable Doped Silver Films

Tom George

Electrical Engineering, San Jose State University

NNIN REU Site: Lurie Nanofabrication Facility, University of Michigan, Ann Arbor, MI

NNIN REU Principal Investigator: Professor L. Jay Guo, Electrical Engineering and Computer Science, University of Michigan

NNIN REU Mentor: Cheng Zhang, Electrical Engineering and Computer Science, University of Michigan

Contact: tom.george@sjsu.edu, guo@umich.edu, chengzh@umich.edu

Abstract:

Silver's low resistivity, high conductivity, and low loss in the visible and near-infrared (NIR) regions makes it perfect for many optoelectronic applications. However, pure silver deposited on a dielectric substrate is unstable, rough, and requires a thick layer to form a continuous film. Aluminum (Al)-doped silver has been shown to circumvent these issues and provide an ultrathin and low loss film with sub-nanometer roughness. This makes Al-doped silver (Ag) a viable alternative to indium tin oxide (ITO) as a flexible transparent conductor. With the benefits of Al-doped Ag known, the purpose of this project was to co-sputter other metals with Ag and observe the results. The roughness, resistivity, and optical properties of these different doped Ag films were measured and a comparison study was performed to compare their properties to that of Al-doped Ag.

Introduction:

Low loss in the visible and NIR regions makes Ag advantageous for use in many optoelectronic and metamaterial applications. However, the Volmer Weber growth of Ag on dielectric substrates and instability at room temperature results in a rough surface [1]. This significantly reduces Ag's use in many devices and makes it difficult to achieve an ultrathin and smooth film.

To circumvent these issues, a 1-2 nm germanium (Ge) seeding layer can be used resulting in Ag films with a smooth surface [1]. However, seeding layers are undesirable for low loss optical applications. This is especially true for Ge, because it is a low band gap semiconductor. Other methods to achieve stable and smooth Ag thin films have been proposed, but are either too optically lossy or too expensive and time consuming.

A way to create ultrathin, smooth, and stable Ag films with minimal time and cost has been shown by using Al in a co-deposition process with Ag. Al is co-sputtered along with Ag and this reduces the percolation threshold to 6 nm with an RMS roughness less than 1 nm for a 15 nm thick Al-doped Ag film [2]. This is a significant reduction from a pure 15 nm thick Ag film, which has a percolation threshold of 10-20 nm and an RMS roughness of about 6 nm [2].

With the knowledge that Al-doped Ag results in an ultrathin, smooth, and stable thin film, we created titanium (Ti)-doped Ag and chromium (Cr)-doped Ag films and investigated their properties. In this work, we compare the properties of the Ti- and Cr-doped Ag films to Al-doped Ag films.

Theory:

Metals, such as Al, affect the nucleation growth of Ag on dielectric substrates such as silicon dioxide (SiO_2). When Al and Ag are co-sputtered together, the strong bond Al has with oxygen from SiO_2 forms a high density of

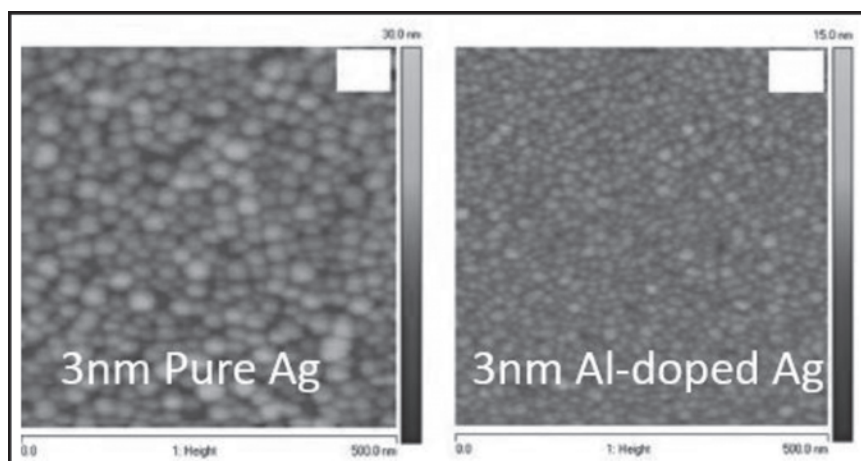


Figure 1: Nucleation sites.

nucleation sites on the surface of the SiO₂ substrate [1]. This acts as a seeding layer from which Ag can easily grow. This enhanced density of nucleation sites has been viewed from a 3 nm thick layer of Ag and Al-doped Ag deposited on SiO₂ as seen in Figure 1.

It is clearly seen that Al-doped Ag has a significantly larger number of nucleation sites compared to Ag deposition.

Along with an enhanced nucleation layer another benefit of co-sputtering with a metal is the formation of a capping layer. After deposition, when the sample is brought out into an oxygen ambient, there is a sudden in-diffusion of O₂ and an out-diffusion of Al, which results in a capping layer [1]. The benefit of a capping layer is that it prevents de-wetting, the agglomeration of Ag, and stabilizes the thin film. It is this combination of an enhanced nucleation layer and a capping layer that results in an ultrathin, smooth, and stable film.

Experimental Procedure:

Samples were made using diced <100> Si and fused silica resulting in 1 cm × 1 cm substrates to deposit on. Using a Kurt J Lesker Lab18 sputtering tool, recipes were created to perform Ti-Ag and Cr-Ag co-sputtering, resulting in Ti-doped Ag and Cr-doped Ag films. During deposition, the Ag target power was kept at a fixed value, while the Ti and Cr targets were varied from a low to high power. The purpose of this was to find the optimal power value to run the Ti and Cr targets that resulted in the least amount of optical loss from the thin film sample. After deposition, thickness and optical measurement were performed using the J.A Woollam ellipsometer. An atomic force microscope (AFM) was then used to provide surface roughness measurements while an SEM was used to observe film grain and continuity.

Results and Discussion:

The results from the Ti-doped Ag and Cr-doped Ag films showed that both metals did promote the growth of thin silver films just like Al. However, both films were inferior to Al-doped Ag films during initial testing.

The 9 nm thick Ti-doped Ag film resulted in an RMS surface roughness of 0.549 nm, with a sheet resistance of 51 Ω/sq, while the 9 nm thick Cr-doped Ag film was 0.709 nm and 25 Ω/sq, respectively. Comparatively, a 9 nm thick Al-doped Ag film has an RMS surface roughness of 0.6 nm with a sheet resistance of 24 Ω/sq.

Acknowledgments:

I would like to thank my mentor Cheng Zhang and my PI Professor Jay Guo for all they have taught me this summer. Also, to Sandrine Martin, Pilar Herrera-Fierro, Nadine Wang, Dhruv Mevada, and Christian Manlutac for their guidance and support. This work would have been impossible without the LNF staff especially David Sebastian. I am grateful to the NNIN REU Program and the National Science Foundation for providing this opportunity (under Grant No. ECCS-0335765).

References:

- [1] Zhang, C., Zhao, D., Gu, D., Kim, H., Ling, T., Wu, Y.-K. R. and Guo, L. J. (2014), An Ultrathin, Smooth, and Low-Loss Al-Doped Ag Film and Its Application as a Transparent Electrode in Organic Photovoltaics. *Adv. Mater.*, 26: 5696-5701. doi:10.1002/adma.201306091
- [2] Gu, D., Zhang, C., Wu, Y.-K. R. and Guo, L. J. (2014), Ultrasoft and Thermally Stable Silver-Based Thin Films with Subnanometer Roughness by Al Doping, *ACS Nano* 2014 8 (10), 10343-10351.

Diblock Copolymers for Diamond Patterning and Applications

Lorelis González López

Chemical Engineering, University of Puerto Rico-Mayagüez

NNIN REU Site: Howard Nanoscale Science and Engineering Facility, Howard University, Washington, DC

NNIN REU Principal Investigator: Dr. Gary L. Harris, Electrical Engineering, Howard University

NNIN REU Mentor: Dr. Michelle Chavis, Material Science and Engineering, Howard University

Contact: lorelis.gonzalez@upr.edu, gharris1124@gmail.com, mac238@cornell.edu

Abstract:

Nitrogen-vacancy (NV^-) centers have been recently forecasted as possible quantum bits — the fundamental unit of quantum information. Their properties include long spin lifetimes and the ability to store quantum information and transmit it in the form of light [1]. However, interaction with their environment leads to decoherence in the presence of nearby nitrogen spins. The key to enhancing NV^- centers is to control their location and reduce their interaction with the environment. Here, we present an innovative method that allows for control over the size and location of diamond nanopillars (DNPs). A hot filament chemical vapor deposition (HFCVD) reactor was used to grow polycrystalline diamond on silicon wafers. The diblock copolymer poly(styrene)-*block*-(2-vinyl pyridine) (PS-*b*-P2VP) was used to create a mask that directs the location and size of the DNPs. Reactive ion etching (RIE) was then used to transfer the patterns from the mask to the underlying substrate. We achieved ~ 10 nm sized diamond nanopillars, which were characterized using atomic force microscopy (AFM) and scanning electron microscopy (SEM).

Introduction:

Nitrogen-vacancy (NV^-) centers are point defects found in diamond that consist of a nitrogen substitutional atom that is adjacent to a lattice vacancy. These NV^- centers have recently emerged as a potential candidate for qubits, the basic information unit for quantum computers. Their unique optical and spin properties makes them attractive for applications in areas such as magnetometry, biomedicine and spintronics [2]. The challenge when working with NV^- centers is that they can easily decohere (lose quantum state) when there are other defects close by. In order to enhance the NV^- center's properties, interaction with the environment must be reduced by keeping them separate.

A fabrication process employing diblock copolymers (DBCP) was developed to create diamond nanopillars (DNPs) as a way to isolate NV^- centers. DBCPs are macromolecules that consist of two polymers covalently linked that self-assemble into various equilibrium ordered nanostructures upon annealing. The DBCP used, poly(styrene)-*block*-(2-vinyl pyridine) (PS-*b*-P2VP) was dissolved in a selective solvent for one block and a precipitant for the other, forming micellar aggregates. These micelles consist of a condensed core of the insoluble block surrounded by a swollen shell of the soluble block in solution phase. The micelles offer advantages for surface modification because they are individual nanoscale entities that can be easily coated over many types of substrates. [3]

The array can be switched between two complementary surface topographies simply by changing the selective solvent used.

Materials and Methods:

Monolayers of PS-*b*-P2VP (91,500-*b*-105,000 g/mol, PDI 1.1) micelles (PS matrix, P2VP core) were created by spin coating a 0.5 wt% solution in toluene at 2000 rpm for 60 seconds on a clean silicon substrate. The substrate was then dipped in methanol, a selective solvent for P2VP, and an inversion of the polymer film forms, P2VP matrix and a PS core.

Reactive-ion etching (RIE) (Plasma-Therm 790) was used to transfer the pattern created by the polymer film into the underlying silicon substrate. The inverted thin film was exposed to a five second oxygen (O_2) etch that removed the PS block, leaving holes in the P2VP matrix layer that reached the underlying silicon substrate. The sample was then further subjected to a sulfur hexafluoride (SF_6) etch (2½ min, 55W, 187.5 mT), which allowed the exposed silicon to be etched, thus creating holes in the substrate.

Poly-crystalline diamond was grown on the etched substrate via a hot filament chemical vapor deposition (HFCVD) process. The silicon substrates were first cleaned with acetone, methanol and toluene and then

seeded by sonicating in a methanol:nanodiamond seed (1:1) solution. The diamond was grown at a filament temperature of 2300°C and a substrate temperature of 750°C with a ratio of hydrogen to methane of 80:1, for three hours.

The diamond surface was then waxed onto a SiC substrate to remove the silicon substrate and expose the DNPs grown inside the substrates' holes. A wet etch solution was used to etch away the silicon substrate completely. The wet etch solution consisted of a hydrofluoric and nitric acid aqueous solution in a 2:2:3 ratio.

Results and Conclusions:

PS-*b*-P2VP was successfully used as a mask to create DNPs with tunable size and distribution. Figure 1 shows an AFM image of the micelles formed (P2VP core) after an O₂ etch to remove the PS matrix. Next, a film of similar characteristics was dipped into a methanol bath, which inverted the core and matrix. After O₂ and SF₆ etches, ~ 15 nm deep holes were obtained on the silicon substrate, as seen in Figure 2. A poly-crystalline diamond layer was grown on the silicon substrate by HFCVD and then transferred to a silicon carbide substrate with a wet etch method. We achieved DNPs with a diameter of approximately 10 nm (Figure 3), which are several orders of magnitude smaller than what can be currently found in literature. Smaller sized DNPs increases the possibility of having just one NV center per pillar. This would avoid any center interactions, making them more stable and therefore more ideal as qubits.

Future work includes adjusting the RIE parameters to obtain taller DNPs and growing a nitrogen-doped layer of diamond on the substrate to create NV centers.

Acknowledgements:

I would like to thank my Principal Investigator, Dr. Gary Harris, my mentor, Dr. Michelle Chavis, site coordinator, Mr. James Griffin, Mr. Crawford Taylor, and the staff of the Howard Nanoscale Science and Engineering Facility. I would also like to thank the NNIN REU Program, and the NSF for funding, Grant No. ECCS-0335765.

References:

- [1] Hausmann, B. J. M.; et al. *Diam. Relat. Mater.* 2010, 19 (5-6), 621-9.
- [2] Ananyina, O. Y.; Severina, E. V. *Bull. Russ. Acad. Sci. Phys.* 2012, 76 (5), 595-599.
- [3] Krishnamoorthy, S.; et al. *Langmuir* 2006, 22 (8), 3450-3452.

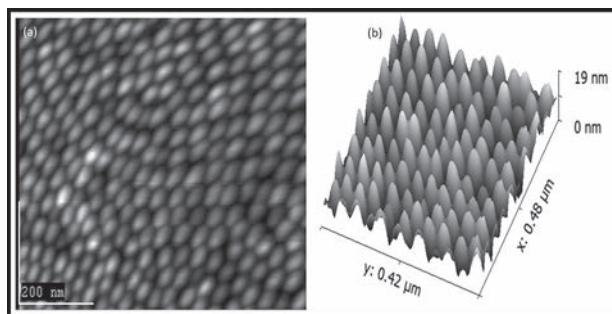


Figure 1: AFM image of (a) PS-*b*-P2VP coated silicon substrate after O₂ etch; (b) corresponding 3D image.

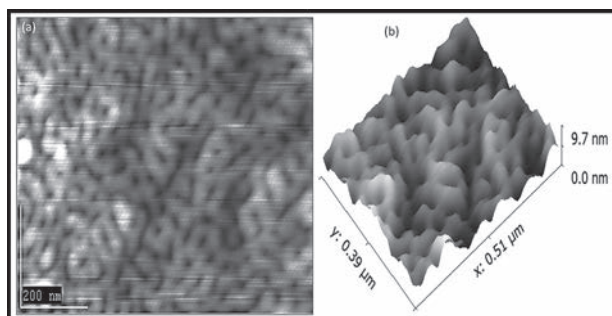


Figure 2: AFM image of (a) PS-*b*-P2VP silicon substrate after O₂ and SF₆ etch; (b) corresponding 3D image.

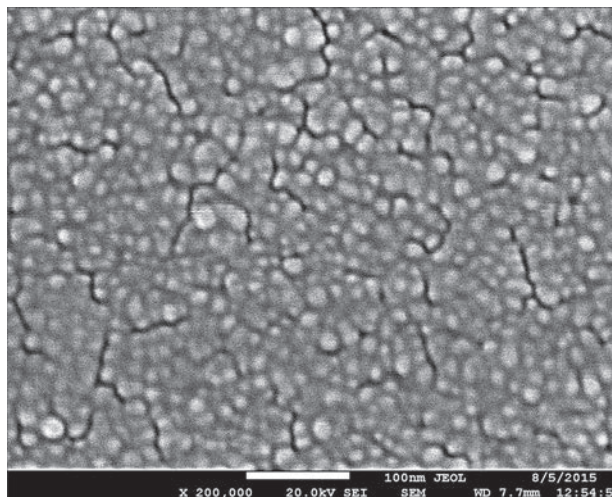


Figure 3: SEM image of diamond nanopillars with an average diameter of 10 nm.

Characterization of Graphene Growth on Pt<111>

Taliya Gunawansa

Optical Engineering, Norfolk State University

NNIN iREU Site: National Institute for Materials Science (NIMS), Tsukuba, Ibaraki, Japan

NNIN iREU Principal Investigator: Dr. Daisuke Fujita, Advanced Key Technologies Division, National Institute for Materials Science

NNIN iREU Mentor: Dr. Keisuke Sagisaka, Surface Characterization Group, Nano Characterization Unit, Advanced Key Technologies Division, NIMS

Contact: t.s.gunawansa@spartans.nsu.edu, fujita.daisuke@nims.go.jp, sagisaka.keisuke@nims.go.jp

Abstract:

Characterization of sizable graphene sheets grown on metal surfaces is key to understanding the interaction between graphene and the substrate for future applications. It is confirmed by Auger electron spectroscopy (AES) and helium ion microscopy (HIM) that graphene was successfully grown on Pt<111> surface through segregation. The graphene consisted of single-layer graphene across the majority of the substrate with various sections of bi- and tri-layer graphene islands and Pt patches. X-ray photoelectron spectroscopy (XPS) reveals the C1s peak from graphene on Pt<111> has lower binding energy than those from graphite (HOPG) and graphene on Ni<111>, suggesting that graphene on Pt<111> has a weaker interaction than other substrates. Topographic images and cross-section data from atomic force microscopy (AFM) depicted that graphene islands are 1.10 nm lower than the surrounding Pt region, in spite of the fact that graphene is grown on Pt. This observation speculated that water adsorption on the Pt region may indicate the nanoscale hydrophobicity of graphene and nanoscale hydrophilicity of Pt<111>.

Introduction:

Graphene, as a single layer of carbon atoms arranged in a honeycomb lattice, has many electronic and physical properties desired for potential applications [1,2]. For graphene to be employed in various prospective applications, large-scale fabrication of graphene on transition metal substrates need to be analyzed [2]. Graphene grown on Pt<111> provided data on the weak bonding interaction with the platinum substrate and aided in the understanding of properties of graphene. Surface segregation of carbon-doped metals has the capability of producing large sheets of graphene on Pt<111>. The produced graphene consisted of a single-layer majority with fractions of bi- and tri-layer graphene islands and platinum sections. Image measurements showed growth of graphene on Pt<111> and suggested a possible relationship between the hydrophobicity of graphene and hydrophilicity of platinum.

Experimental Procedure:

Carbon was doped into a pristine platinum sample by holding the crystal in high purity carbon powder at 800°C in high vacuum for 40 days, which yielded a 0.017 atomic percent concentration of carbon. Afterwards, it was heated to 1000°C for one minute and cooled to prompt segregation of graphene. Figure 1 illustrates the process of surface segregation and the importance of slowly cooling the sample to prompt larger amounts of graphene growth.

Auger electron spectroscopy (AES) was employed to observe growth as well as helium ion microscopy (HIM) since it provided

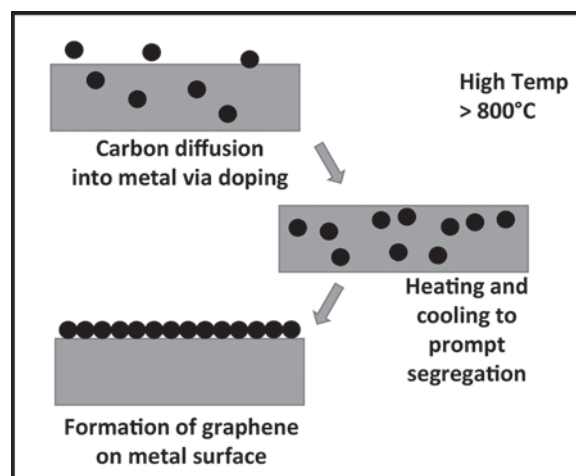


Figure 1: Schematic of segregation method.

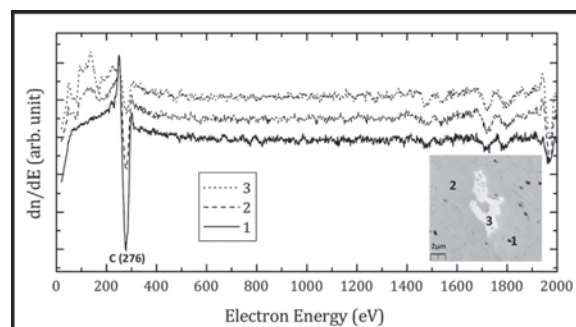


Figure 2: Carbon and Pt peaks (graph) from points 1, 2, and 3 on the SEM image.

better material contrast and depth. The characterization techniques included scanning tunneling microscopy (STM) to measure the surface morphology in the atomic scale, AFM that highlighted the topography, potential and mechanical property distributions, and x-ray photon spectroscopy (XPS) to analyze the interaction between graphene and the substrate.

Results and Conclusions:

Figure 2 represents the scanning electron microscope (SEM) image of the center of the surface and identifies three different point spectroscopy on the sample. The corresponding graph depicts the peaks of carbon and platinum at points 1, 2, and 3. Measurements of the peak heights indicate that section 1 contains the highest amount of carbon and least amount of platinum while section 3 observes the opposite. The data calculates section 2 as having higher quantities of carbon than platinum, leading to the assumption that section 2 is a single-layer sheet of graphene. Element mapping confirmed the assumption and identified section 1 as multi-layer graphene and section 3 as platinum.

Figure 3 shows the binding energy in the carbon peak for graphene grown on Pt<111> as measured with XPS. The

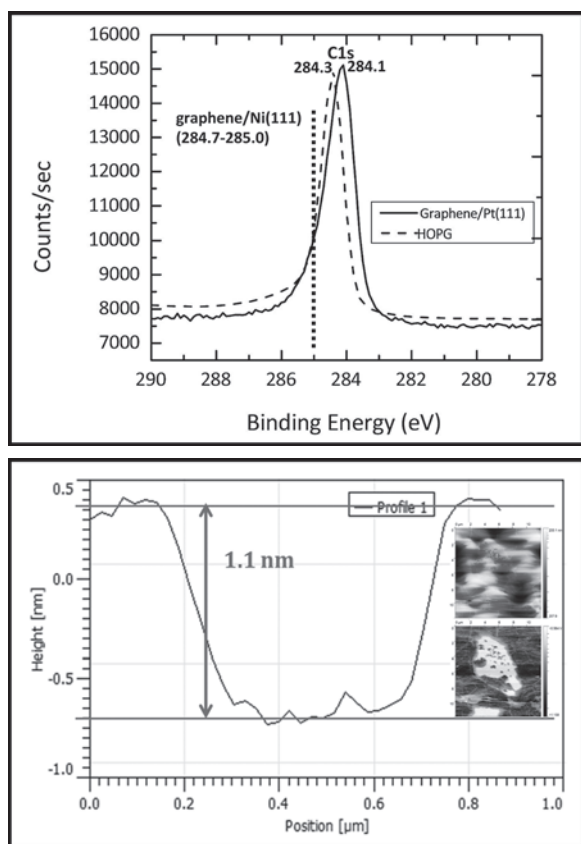


Figure 3, top: Comparison of graphene interaction on Ni<111> and Pt<111>. Figure 4, bottom: Cross section between graphene and Pt (graph), topography (top image), and potential (bottom image).

dash peak represents the higher binding energy of multi-layer graphene, HOPG. Graphene grown on Ni<111> has a range of 284.7 to 285.0 eV, which indicates that nickel has the stronger interaction with graphene [3]. The peak position was sensitive to the environment and changed how graphene settled on the substrate.

Figure 4 portrays the topography and potential of graphene on Pt<111>. The topographic image obtained by AFM proved difficult to distinguish the divisions of graphene and platinum. However, the potential image depicted in the Kelvin probe force microscope mode clearly identifies the dark area to be graphene and the lighter area to be platinum. An interesting observation shows the darker islands of graphene in the topographic image to be lower than the platinum sections, even though graphene was grown on top of the platinum surface. The corresponding graph displays the cross section to determine that the graphene was 1.10 nm lower than platinum on the substrate. The reason for this peculiar observation might be explained by expansion of the platinum sections due to oxidation, since graphene is stable in air while metal surfaces are generally not. However, the possible scenario of an oxide layer being on the surface was excluded due to the lack of oxygen peaks in the Auger data. A more plausible speculation is the formation of water layer on platinum. If a water layer was present on the surface, the conclusion could indicate the hydrophobicity of graphene and hydrophilicity of platinum.

Future Work:

Water admitted on the sample should be considered to clarify the hydrophobicity of graphene and hydrophilicity of Pt to support the experimental data collected thus far. Furthermore, experimental studies regarding graphene grown on Ni<111> should be conducted to compare the shift in energy bonds with XPS imaging.

Acknowledgments:

I sincerely thank my PI, Dr. D. Fujita, and my mentor, Dr. K. Sagisaka, for all of their assistance and guidance. I extend my thanks to Dr. Kusawake, Dr. Masuda, K. Matsushita, S. Nagano, and the National Nanotechnology Infrastructure Network International Research Experience for Undergraduates (NNIN iREU) Program, the National Institute of Material Sciences, and the National Science Foundation, Grant No. ECCS-0335765, for providing the opportunity and funding for this research experience.

References:

- [1] Novoselov, K., et al., Science 306, (5696):666-669, (2010).
- [2] Gao, J., et al., Nanotechnology 23, 055704 (5pp), (2012).
- [3] Fujita, D., et al., American Vacuum Society 12(4), (1994).

Al-Induced Crystallization of Si Thin Films on Flexible Glass Substrates

Sophia Hu

Chemistry, University of Pennsylvania

NNIN REU Site: Penn State Nanofabrication Laboratory, The Pennsylvania State University, University Park, PA

NNIN REU Principal Investigator: Dr. Joan Redwing, Department of Materials Science and Engineering, The Pennsylvania State University

NNIN REU Mentor: Mel Hainey, Jr., Department of Materials Science and Engineering, The Pennsylvania State University

Contact: sophiahu_426@yahoo.com, jmr31@psu.edu, mfh5099@psu.edu

Abstract:

Highly-oriented silicon (Si) films on flexible substrates are attractive for thin-film electronic and energy applications. Ultra-thin flexible glasses are of special interest for substrate use because they offer flexibility and higher thermal stability than polymers. Thus, the goal of this project was to investigate the growth of silicon (Si) films on 50 μm thick flexible glasses, using an aluminum-induced crystallization (AIC) process. AIC lowers the Si crystallization temperature to temperatures below the softening temperatures of the glasses; furthermore, it produces Si films with large grains and preferential orientation. Large-grain polycrystalline Si thin films of 30 nm thick and 100 nm thick were successfully grown on 50 μm thick flexible glass substrates. Films 30 nm thick demonstrated larger grain size but higher electrical resistance than 100 nm thick films. Mechanical flexibility was tested by bending the samples around a tube of radius 5.75 cm, close to the maximum curvature radius of the glass substrate (~ 4.5 cm). Bending caused the samples (glass substrates with Si films on top) to fracture but did not produce any new cracks or delamination in the films themselves; bending also did not change the films' electrical resistance. These results suggested high flexibility of the Si films. In comparison, bare glasses (with no films) did not fracture, further suggesting the Si films added stress to the glass substrates.

Introduction:

Silicon (Si) thin-film technology has garnered widespread attention for its advantageous properties over bulk silicon materials. Compared with bulk Si substrates, Si thin films grown on inexpensive substrates allow for far more cost-effective manufacture and handling of Si devices. Commonly used substrates for Si films include conventional (rigid) glasses and polymers. However, both substrates have drawbacks. While conventional glasses have high thermal stability, they are heavy and inflexible, making installation of these materials difficult and expensive. Polymers are lighter and flexible but have low thermal stability, so they cannot be used for high-temperature or high-power applications [1]. Therefore, research has recently turned to ultra-thin flexible glasses (thickness: ≤ 100 μm), which contain both flexibility and high thermal stability. Si thin films grown on these flexible glasses open up new possibilities for small, lightweight, bendable, and durable devices. Potential applications range from high-efficiency thin-film solar cells to flexible biosensors to scrollable displays.

Aluminum-induced crystallization (AIC) offers a convenient way to grow Si films on flexible glasses. Amorphous Si (α -Si) cannot be deposited directly on glass because the Si crystallization temperature is $\sim 600^\circ\text{C}$, which exceeds the softening temperatures of the glass

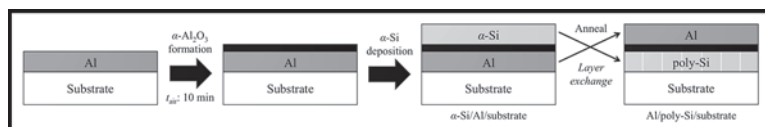


Figure 1: Schematic of the AIC process.

substrate ($T_g \leq 600^\circ\text{C}$) [2]. The addition of aluminum (Al) lowers the T_g of Si to temperatures below T_g (in this case, 450°C), allowing Si to be crystallized without deforming the glass substrate. Figure 1 illustrates the scheme of the AIC process.

First, Al is deposited on the glass substrate and exposed to air for 10 minutes to form α - Al_2O_3 , which is important for controlling crystal orientation of Si. Si is then deposited on top. Annealing causes Si atoms to diffuse through the Al_2O_3 layer into the Al layer, and Al atoms are pushed to the top. This results in complete layer exchange of Al and Si, giving rise to Si films with large grains and preferential orientation [3].

Experimental Procedure:

Al films were deposited (thicknesses: 30 and 100 nm, deposition rate: $1.5\text{\AA}/\text{s}$) onto flexible glasses (Nippon Electric Glass, OA-10G 50 μm) via electron-beam evaporation. The films were exposed to air for 10 minutes

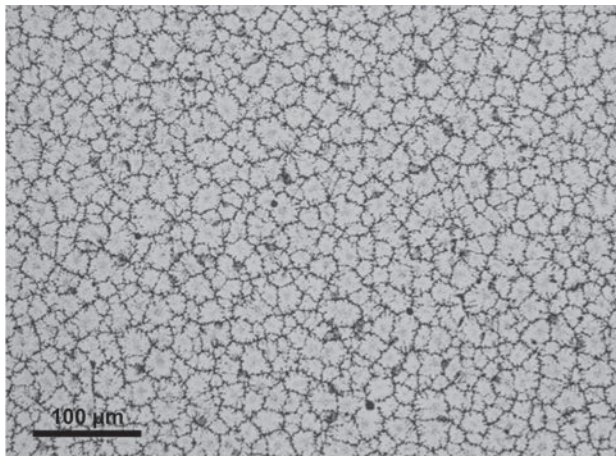


Figure 2: Optical microscopy image of 30 nm thick Si film.

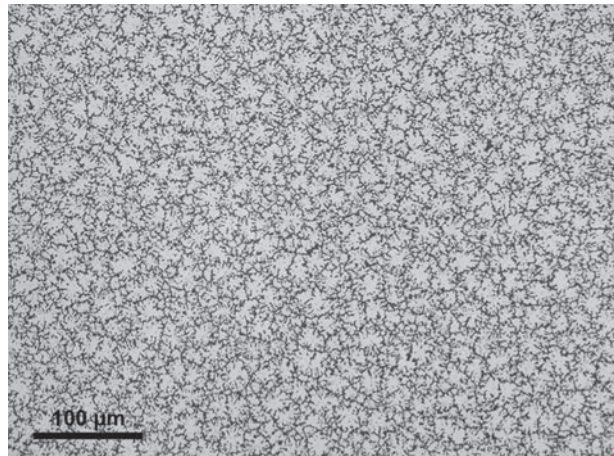


Figure 3: Optical microscopy image of 100 nm thick Si film.

to form $\alpha\text{-Al}_2\text{O}_3$. Amorphous Si films, with identical thicknesses as Al, were deposited on top. The samples were annealed at 450°C (4 hours for 30 nm films, and 10 hours for 100 nm films) in N_2 to cause AIC. Al was etched off with Aluminum Etch Type A.

Morphology and electrical resistance of the films were characterized by optical microscopy and ohmmeter measurements. Mechanical flexibility was tested by bending the samples eleven times on each side (alternating between each side) around a tube of radius 5.75 cm. Changes in morphology, such as cracks or delamination, were observed via optical microscopy. Bare glasses (with no films), annealed under identical conditions, were also bent eleven times on each side for comparison.

Results and Conclusions:

Si films with thicknesses of 30 nm and 100 nm were successfully grown on 50 μm thick glasses via AIC. Optical microscopy demonstrated the films to be polycrystalline and large-grained. The 30 nm films (Figure 2) had a grain size of $\sim 16 \mu\text{m}$, while the 100 nm films (Figure 3) had a slightly smaller grain size of $\sim 14 \mu\text{m}$. Using an ohmmeter, the 30 nm films were measured to have a resistance of $\sim 3\text{-}5 \text{ M}\Omega$, and the 100 nm films had a resistance of $\sim 130 \text{ k}\Omega$.

Bending the samples (glass substrates with Si films coated on top) up to a total of eleven times fractured them into a few pieces, but produced no additional cracks or other new changes in the films themselves. Electrical resistance of the films was not changed either. The lack of change in morphology or electrical resistance suggested high flexibility of the Si thin films.

The flexibility of the samples was compared with that of bare glasses (with no films). The bare glasses, annealed under identical temperatures and durations, did not fracture in the bending tests. This suggested that the Si films, while highly flexible, added stress to the glass

substrates, causing them to become more brittle than the bare glasses. Introduction of internal compressive stress by Al during annealing might explain this additional stress on the glasses [4]. However, cracks at the edges of the glass substrates and defects (e.g., black spots) in the films were observed prior to bending and could have made the samples more fragile, thus distorting the bending test results.

Future Work:

Further investigation into the flexibility of the Si films, especially possible external factors in the bending tests, will be necessary. External factors, such as cracks (from cutting the glasses, cleaning, and handling) and stress from metal tweezers, could have made the samples more fragile and prone to breaking. Plastic tweezers are softer than metal tweezers and will be used instead in the future. In addition, the Si films were not “clean-looking” and contained defects, which were likely caused by contamination from the surrounding environment. Screening out such external factors in the bending tests will help assess the flexibility of the Si films more accurately.

Acknowledgments:

I would like to thank Mel Hainey, Jr., and Dr. Joan Redwing for their mentorship and support in the lab. I am also thankful to the Penn State Nanofabrication Laboratory staff and the NNIN REU Program. This research was made possible by the National Science Foundation (NSF) under Grant No. ECCS-0335765.

References:

- [1] Manoharan, M. P.; et al., *Energy Technol.* 2013, 1, 313-318.
- [2] Gall, S. In “Crystal Growth of Silicon for Solar Cells”; Nakajima, K.; Usami, N., Eds.; Springer Berlin Heidelberg: Berlin, Germany, 2009; pp 193-218.
- [3] Kurosawa, M. et al., *Appl. Phys. Lett.* 2009, 95, 132103.
- [4] Hekmatshoar, B. et al., *J. Vac. Sci. Technol., A.* 2004, 22, 856.

Investigation of the Thermoelectric Properties of Boron Carbide-Hafnium Diboride Composite Materials

Jon-L Innocent-Dolor

Chemical Engineering, Syracuse University

NNIN iREU Site: National Institute for Materials Science (NIMS), Tsukuba, Ibaraki, Japan

NNIN iREU Principal Investigator: Prof. Takao Mori, International Center for Materials Nanoarchitectonics, National Institute for Materials Science

NNIN iREU Mentor: Dr. Satofumi Maruyama, International Center for Materials Nanoarchitectonics, National Institute for Materials Science

Contact: jcinnoce@syr.edu, mori.takao@nims.o.jp, maruyama.satofumi@nims.go.jp

Abstract and Introduction:

In primary energy conversion, it is estimated that only about one-third of the total energy used becomes useful work. Of the two-thirds wasted, the majority is in the form of heat. Thermoelectric modules can be used to directly convert some of this waste heat back to effective use, thus, improving the overall conversion efficiency. Thermoelectric materials research has experienced a renewed interest in recent years as several new candidate materials are being discovered and optimized. One class of materials that have emerged for use in high temperature thermoelectric applications is borides. Borides such as boron carbide exhibit several favorable mechanical and thermoelectric properties such as high thermal and chemical stability, and a Seebeck coefficient that increases with temperature. The thermoelectric performance of borides can be improved by using composites – usually metal borides [1]. In this work, the effect of hafnium diboride composition on the thermoelectric properties of boron carbide was studied.

Boron carbide-hafnium diboride (B_4C/HfB_2) composites were prepared by spark plasma sintering (SPS) of a mixture of hafnium diboride powder and boron carbide powder. The boron carbide powder was prepared with a 13.3 wt% composition of carbon, which a previous study found to be the ideal carbon content for the dimensionless figure of merit [2]. The hafnium diboride content was varied between 0 and 20 percent by weight and the effect on the thermoelectric properties was studied. The samples were characterized using x-ray diffraction (XRD). The electrical resistivity and Seebeck coefficient were measured using the four-probe method and differential method, respectively. The thermal conductivity was measured by the laser flash method. The optimal hafnium diboride content was found to be 10 wt%, leading to an improvement in the figure of merit ZT from 0.188 for the non-composite material to 0.200 for the 10% wt HfB_2 composite at 730°C.

Experimental:

Firstly, B_4C powder was prepared with a 13.3 wt% composition of carbon by heating of a boron and carbon powder mixture in an induction tube furnace. This B_4C powder was then mixed with HfB_2 powder to create 0, 5,

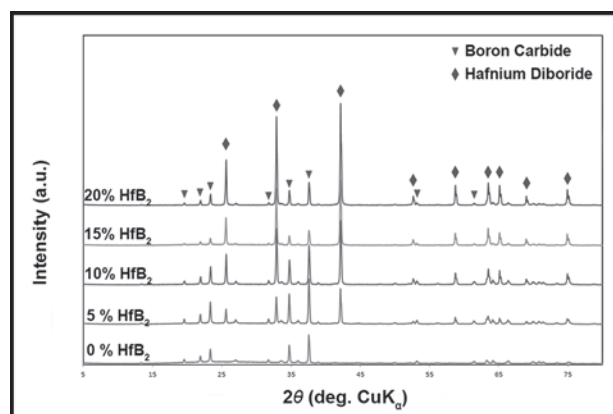


Figure 1: X-ray diffraction data for composite samples showing relative peak heights.

10, 15 and 20% HfB_2 by weight samples. The powder was weighed out into 0.7 g samples for sintering and placed into a graphite dye. A SPS system was then used to sinter the composite powders at 1750°C. The sintered pellets were then polished and cut for thermoelectric measurements.

The electrical resistivity was determined by the four-probe method, while the Seebeck coefficient was measured by the differential method. We then used the laser flash method to determine the thermal conductivity of the samples. The samples were ground into a powder for XRD measurements in order to characterize their compositions.

Results and Discussion:

The XRD measurements (Figure 1) were used to confirm the composition of the samples based on the peak positions, and height. In addition, the lack of a shift of peak position for each sample indicates that the crystal structure is not affected by the addition of HfB_2 .

For all compositions, the Seebeck coefficient first decreases with temperature, then increases with temperature beyond approximately 480°C (Figure 2). The increasing Seebeck coefficient with temperature beyond this point makes boron carbide a favorable material for high temperature applications. It can be seen from Figure 1 that the Seebeck

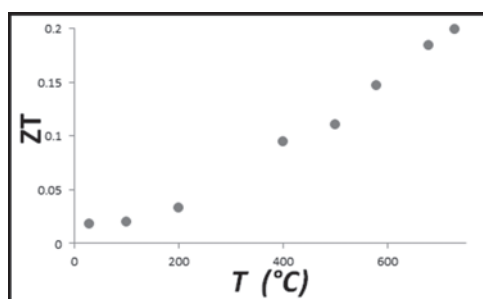
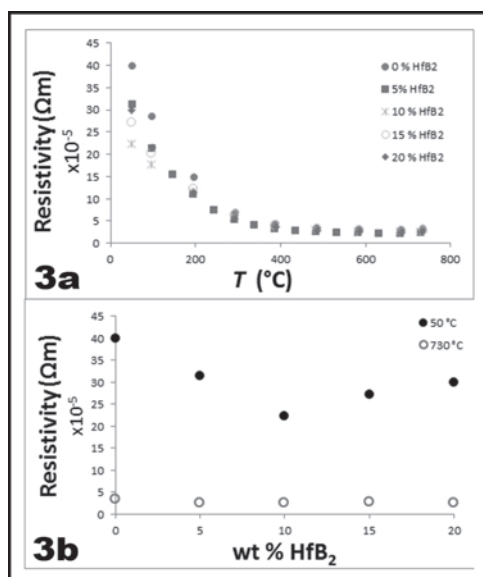
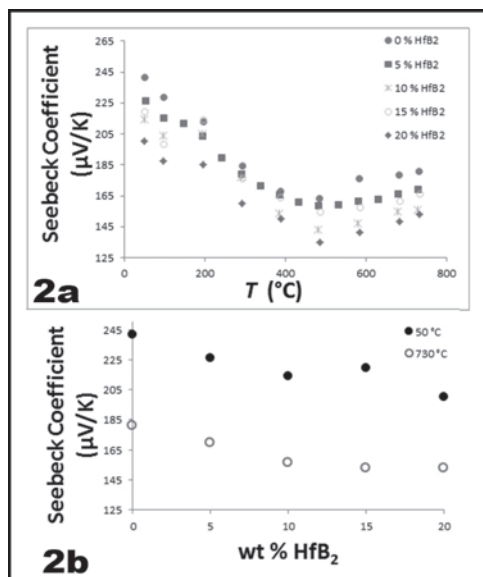


Figure 2, top: Seebeck coefficient as a function of a) temperature, and b) HfB₂ composition.

Figure 3, middle: Electrical resistivity as a function of a) temperature, and b) HfB₂ composition.

Figure 4, bottom: Thermoelectric figure of merit ZT as a function of temperature for 10% HfB₂ sample.

coefficient decreases with increasing HfB₂ composition. This is expected because boron carbide is being replaced by a material with a lower Seebeck coefficient, therefore the overall composite material should have a lower Seebeck coefficient.

Similarly, the electrical resistivity of the samples was compared with changing temperature and composition (Figure 3). The electrical resistivity was found to decrease with temperature for all the compositions examined. The electrical resistivity decreases with increasing HfB₂ content up to 10 wt%, then increases. This result is unusual because the resistivity would be expected to continuously decrease with increasing HfB₂ composition. However, we believe the density of the samples, which was lower than would be expected, is to blame. Further work will be done in order to explain this anomaly.

The thermal conductivity was found to decrease with increasing HfB₂ composition. At 100 $^{\circ}\text{C}$, the thermal conductivity was found to be 4.56 W/mK, 4.52 W/mK and 4.28 W/mK for the 0%, 5% and 10% samples, respectively.

The thermoelectric figure of merit ZT (Figure 4) was found to be the highest for the 10 wt% HfB₂ sample. The ZT value for each sample was found to still be increasing with temperature within the range investigated. The ZT value was increased from 0.188 for the non-composite material to 0.200 for the 10% wt HfB₂ composite at 730 $^{\circ}\text{C}$, an increase of 6%.

Conclusions and Future Work:

The addition of hafnium diboride to boron carbide to form a composite material is a viable means of improving the thermoelectric performance of boron carbide. The measurements show that with an optimum composition, the decrease in the value of the Seebeck coefficient caused by the addition of HfB₂ is countered by the relatively larger decrease in both thermal conductivity and electrical resistivity. The results also show that boron carbide has excellent potential as a high temperature thermoelectric material as the Seebeck coefficient increases with temperature while the thermal conductivity and electrical resistivity decrease with temperature, which leads to a ZT value that increases with temperature.

In the future we hope to fine-tune the optimum composition of hafnium diboride by creating samples that vary by smaller increments of HfB₂ composition. We would also like to measure the thermoelectric properties at higher temperatures as the ZT value is still increasing within the temperature range investigated.

Acknowledgements:

I would like to thank the National Science Foundation and the National Nanotechnology Infrastructure Network International Research Experience for Undergraduates (NNIN iREU) Program for funding and support of this research (under Grant No. ECCS-0335765).

References:

- [1] Feng, B., H.-P. Martin, and A. Michaelis. J of Elec Mats (2013): 2314-319.
- [2] Bouchacourt, M., and F. Thevenot. J of Materials Science: 1237-247.

Carbon Materials Assisted ZnO Nanowire Array Composites for Enhanced Photoelectrochemical Water Oxidation

Samantha Kang

Mechanical Engineering, University of Washington

NNIN iREU Site: National Institute for Materials Science (NIMS), Tsukuba, Ibaraki, Japan

NNIN iREU Principal Investigator: Professor Jinhua Ye, International Center for Materials Nanoarchitectonics (MANA), Environmental Remediation Materials Research Unit, NIMS, Tsukuba, Ibaraki, Japan

NNIN iREU Mentor: Li Mu, Catalytic Materials Group, MANA, NIMS, Tsukuba, Ibaraki, Japan

Contact: kangsam7@uw.edu, jinhua.ye@nims.go.jp, li.mu@nims.go.jp

Abstract:

In an effort to enhance water oxidation kinetics, ternary structured zinc oxide nanowire (ZnO NW) array composites were investigated. ZnO NW arrays were grown via hydrothermal synthesis, electrodeposited with cobalt oxide (Co_3O_4) as the co-catalyst, and then loaded with carbon materials to achieve hierarchical ZnO- Co_3O_4 -carbon NW structures to prevent electron-hole recombination and increase oxidation reaction rates. Initial PEC testing indicates that adding a co-catalyst and multi-walled carbon nanotubes (CNTs) enhances PEC water oxidation currents when compared to pristine ZnO NW photocurrents. At a potential of 0.6 V vs. Ag/AgCl (1.23 V vs. RHE), the PEC water oxidation current of ZnO- Co_3O_4 -CNT NW arrays measured was 1.61 mA/cm², which is nearly double the photocurrent achieved by pristine ZnO NWs (0.8618 mA/cm²). These results demonstrate that the Co_3O_4 co-catalyst in combination with CNTs promote electron-hole pair charge separation, a feature essential for water oxidation. Lastly, hierarchical graphene oxide-ZnO- Co_3O_4 NW array composites were fabricated to study how 1D-ZnO-2D-GO- Co_3O_4 influences the photoelectrochemistry of water oxidation.

Introduction:

Achieving total photoelectrochemical (PEC) water splitting can help combat the energy crisis by providing clean alternative fuels. However, total water splitting is difficult due to the slow reaction rates of the water oxidation half reaction and rapid recombination of photogenerated electron-hole pairs in semiconductor photocatalytic materials [1]. Using the PEC approach, we can separate the total water splitting reaction into its redox half-reactions. To suppress electron-hole recombination and accelerate water oxidation kinetics, carbon materials such as CNTs and a Co_3O_4 co-catalyst were hierarchically added to the ZnO semiconductor photocatalyst to achieve enhanced PEC water oxidation [2].

Experimental Methods:

Fabrication of Ternary Structured ZnO Nanowires. The ZnO NWs were grown via hydrothermal synthesis [2]. As seen in Figure 1A, conductive fluorine-doped tin oxide (FTO) substrates were spin-coated five times with 0.01 M Zn acetate seed solution and then annealed at 350°C for 30 minutes. The substrates were then vertically suspended in a Teflon® autoclave, in 0.06 M $\text{Zn}(\text{NO}_3)_2$ and HMT solution, for 24 hours at 110°C to synthesize ZnO NWs [3]. The NWs were then rinsed with deionized (DI) water and dried in air. Next, the substrates were electrodeposited with 0.06 M CoCl_2 (aq) at -1 mA for 10 seconds, rinsed with DI water, and dried in air. The substrates were then soaked

in aqueous CNT solution (0.25 mg/mL, functionalized with 3:1 $\text{H}_2\text{SO}_4/\text{HNO}_3$ mixture) for 20 seconds and then annealed for two hours at 300°C. Figure 1B shows the intended ZnO- Co_3O_4 -CNT NW structure.

PEC Water Splitting Set Up. Linear sweep voltammetry (current-voltage and current-time) tests were conducted to analyze and compare the photoelectrochemical activity of pristine ZnO NWs, binary ZnO- Co_3O_4 and ZnO-CNT NWs, and ternary structures. All experiments were conducted using AM 1.5G simulated sunlight in aqueous 0.5 M Na_2SO_4 (pH of 6.8) solution, using a saturated Ag/AgCl reference electrode and platinum counter electrode. Measurements were conducted at a scan rate of 10 mV/s over a potential range of -0.3 V to 1.2 V vs. Ag/AgCl. Figure 3 shows the PEC cell testing set up in which the ZnO- Co_3O_4 -CNT hierarchical NWs act as the photoanode where water oxidation occurs.

Results:

X-ray diffraction tests (Figure 2A) confirmed that the main peak at a 2θ value of 35.1° can be indexed to the <002> crystal phase, which confirms preferential <001> ZnO NW growth on the FTO substrate [2]. The effects of hierarchically adding a co-catalyst and CNTs to the ZnO NWs are clearly shown in the PEC current-time ON-OFF illumination cycle plots (see Figure 3A,B). In Figure 3B at 0.6 V

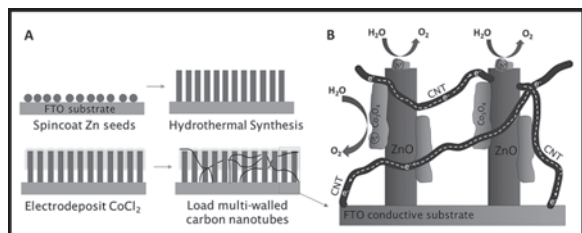


Figure 1: ZnO NW synthesis; ternary structure.

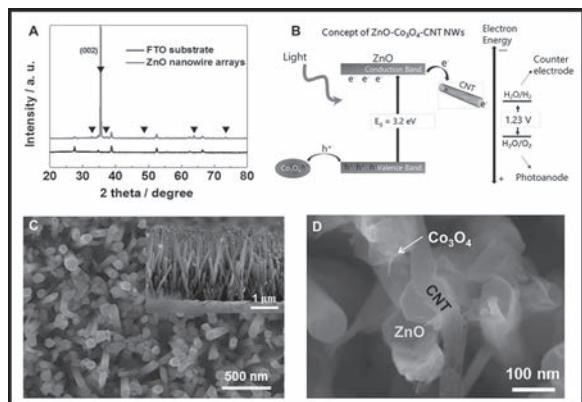


Figure 2: (A) XRD pattern. (B) Bandgap concepts. (C) ZnO NWs. (D) ZnO-Co₃O₄-CNT NWs.

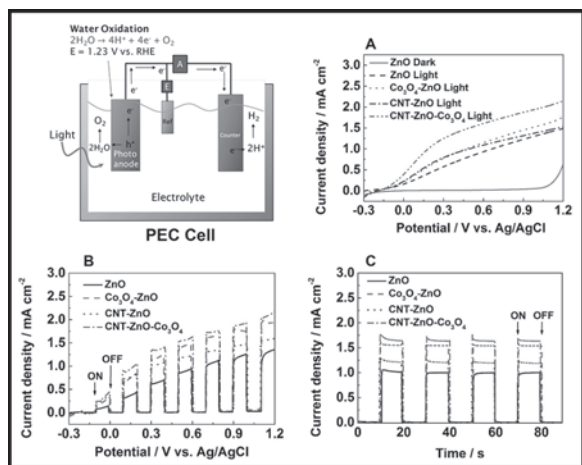


Figure 3: (A-C) PEC results.

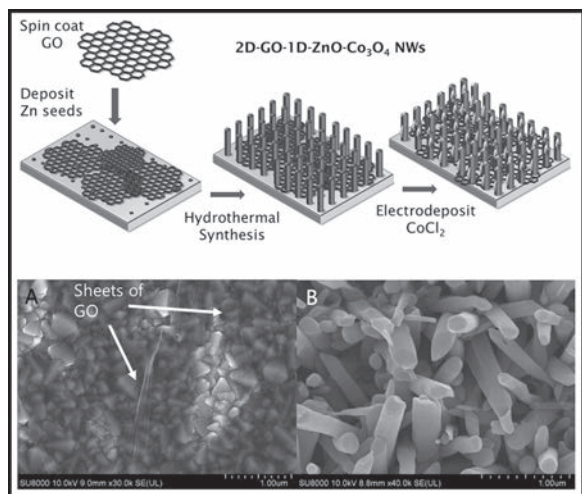


Figure 4: GO-ZnO-Co₃O₄ NW synthesis. (A) GO on FTO. (B) ZnO on GO-FTO.

potential (~ 1.23 V vs. RHE), the PEC water oxidation current density achieved by the ternary structures is 1.61 mA/cm², which is nearly double the current density achieved by pristine ZnO NWs (0.862 mA/cm²).

These results also show that ZnO-Co₃O₄-CNT structures exhibit enhanced photoelectrochemical response, which means the Co₃O₄ co-catalyst acts as an effective oxidation site (where holes oxidize H₂O) that accelerates water oxidation kinetics, and the CNTs act as bridges for electrons to transport to the conductive substrate, thus preventing rapid electron-hole recombination. This concept (Figure 2B) explains why our photocurrent densities (ZnO-Co₃O₄-CNT > ZnO-Co₃O₄ > ZnO-CNT > ZnO) are enhanced with the ZnO ternary structure.

Conclusion and Future Work:

Ternary structured ZnO NWs were successfully fabricated in which the PEC water splitting results indicate that ZnO-Co₃O₄-CNT NW array composites enhance PEC water oxidation kinetics by improving photogenerated charge separation dynamics and electron transfer efficiency.

Novel ternary graphene oxide-ZnO-Co₃O₄ NW structures were also fabricated. Similar to how the CNTs act as bridges for enhanced electron transfer to the conductive substrate, we hypothesized that adding 2D graphene oxide (GO) would facilitate improved charge transfer due to its planar geometry in combination with the ZnO NWs' 1D geometry. The 2D GO-1D ZnO-Co₃O₄ NW array composites were fabricated by first spin coating GO onto FTO substrates (Figure 4). The samples were then spin coated with Zn acetate seed solution and annealed at 350°C in N₂ for 30 minutes to grow Zn seeds. The samples were processed via hydrothermal synthesis at the same preparation conditions as the ZnO-Co₃O₄-CNT NW structures. Initial SEM images (Figure 4A, B) and PEC testing indicate non-uniform GO deposition and ZnO NW growth on FTO substrates must be further investigated to synthesize stable NWs.

Acknowledgements:

I would like to thank the National Science Foundation and the National Nanotechnology Infrastructure Network International Research Experience for Undergraduates (NNIN iREU) Program for funding and support of this research (under Grant No. ECCS-0335765). Also, special thanks to my PI Professor Jinhua Ye, my mentor Li Mu, and the Catalytic Materials Group at the National Institute for Materials Science.

References:

- [1] Y. Tachibana, L. Vayssieres, J. Durrant, Nature Photonics, Vol. 6, no., pp. 511-518, 31 July 2012.
- [2] M. Li, K. Chang, J. Ye, Journal of Materials Chemistry, Vol.3, no., pp. 13731-13737 2015.
- [3] H. M. Chen, C. K. Chen, and K.-H. Chen, Angew. Chem. Int. Ed., 2010, 49, 5966-5969.

Fundamental Studies of the Synthesis of Graphene Using Plasma Enhanced Chemical Vapor Deposition Processes

Yasunori Kutsuma

The School of Science and Technology, Kwansei Gakuin University, Japan

NNIN iREG Site: Institute for Electronics and Nanotechnology, Georgia Institute of Technology, Atlanta, GA

NNIN iREG Principal Investigator: Prof. Eric M. Vogel, Material Science and Engineering, Georgia Institute of Technology

NNIN iREG Mentors: Christopher Perini and Brian Beatty, Material Science and Technology, Georgia Institute of Technology

Contact: amb81817@kwansei.ac.jp, chrisperini@gatech.edu, bbeatty7@gatech.edu

Abstract and Introduction:

Graphene, the two-dimensional form of carbon, has a linear electronic dispersion with high electronic mobility. Much research has utilized graphene in high performance devices to realize practical applications [1]. However, these innovative devices require large, uniform and high crystallinity graphene sheets. In plasma enhanced chemical vapor deposition (PECVD), the decomposition process of hydrocarbon atoms is facilitated by the plasma as opposed to by thermal decomposition, allowing for low temperature synthesis [2]. This is the reason that PECVD growth is well suited for the mass production of graphene wafers.

Low crystallinity of graphene grown using PECVD is a barrier to realize practical applications [1]. D. A. Boyd, et al., improved PECVD graphene synthesis by using a mixed gas of nitrogen and methane in hydrogen plasma [3]. They claimed high quality graphene synthesis was achieved with copper etching by CN^{\cdot} radicals. In addition, the bottom side of copper foils was used to grow graphene to inhibit the direct plasma exposure. High quality graphene synthesis was achieved at low temperature. The nitrogen has an impact pre growth, but the role during growth is not understood. In this study, we investigated the synthesis of graphene using PECVD with nitrogen to realize reproducible synthesis of high quality graphene wafers.

Experimental Procedure:

Growth occurred on the bottom side of copper foils elevated by small silicon wafer pieces in a Black Magic (Aixtron) PECVD furnace. The copper was cleaned before synthesis for 10 minutes under a 700 sccm hydrogen and 100 sccm nitrogen flow at 300°C in a 40W DC plasma. After cleaning, a mixture gas of nitrogen and methane in hydrogen plasma was used for growth with a total

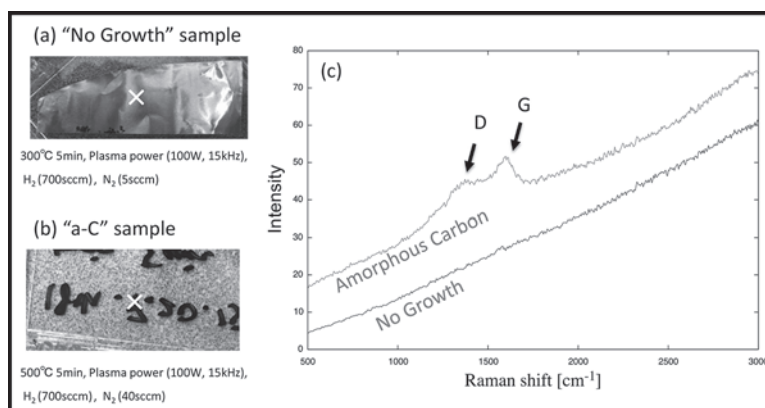


Figure 1: (a) and (b) Optical images after the PECVD growth, and (c) Raman spectra taken from grown samples.

pressure of 23 mbar. Growth temperature ranged from 300°C to 700°C and flow rates of methane and nitrogen were controlled in the range of 5 to 40 sccm. Samples were analyzed with Raman spectroscopy (Thermo Nicolet Aemga XR dispersive Raman utilizing 488 nm laser wavelength).

Results:

The optical images of two samples under different growth conditions are shown in Figure 1(a) and (b). One is an “amorphous carbon (α -C)” sample and the other is a “no growth” sample. Typical Raman spectra are shown in the right side of Figure 1(c). Using these spectra, we evaluated the crystallinity of the deposited carbon on copper foils. At 300°C, no carbon was deposited on the foil, as evidenced by the lack of D (1350 cm^{-1}) and G (1580 cm^{-1}) peaks, whereas at 500°C, α -C was deposited, evidenced by the broad D and G peaks and lack of 2D (2700 cm^{-1}) peak. The cause of the “no growth” condition can be due to either the low adsorption coefficient of carbon species or the existence of carbon etchants.

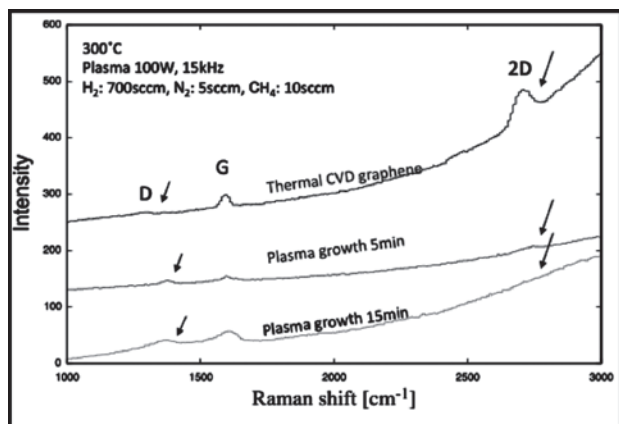


Figure 2: Raman spectra taken from a thermal CVD graphene sample and post plasma growth samples for 5 and 15 minutes.

To verify these possibilities, we put pre-grown thermal CVD graphene samples into the “no growth” condition. The graphene surface was face down and placed on wafer pieces for elevation. Figure 2 shows Raman spectra taken from a thermal CVD graphene sample showing a clear 2D peak and a small D peak. From the Raman spectrum, this graphene is found to have good crystallinity.

This sample was separated into two pieces, and each of them processed in the “no growth” condition for 5 and 15 minutes respectively. As a result, it was found that graphene was etched under these growth conditions, which explain the disappearance of the 2D mode and the appearance of the D peak.

The possible etchants are reactive hydrogen or CN-radicals. In these experiments, the copper foils were etched and deposited on the chamber walls of the PECVD furnace. The primary etchant of copper species in the plasma condition are the CN⁻ radicals. The CN⁻ radicals are generated by a reaction between reactive C and reactive N, reducing the available carbon species for graphene synthesis. Thus, the balance of methane to nitrogen is an important factor to determine the carbon deposition regime. Additionally, hydrogen is known to etch carbon, which also contributes to the carbon deposition regime [4]. In this research, we did not successfully synthesize graphene, but we hypothesize that a transition regime (shown in Figure 3) exists in which graphene growth is possible at low temperatures.

Conclusions and Future Works:

In this research, we attempted to grow graphene on copper foils using the PECVD method with a mixture of nitrogen and methane in hydrogen plasma. We found two regimes: the “carbon etching” regime and the “ α -C deposition” regime. These conditions were achieved by varying the ratio of methane flow to nitrogen flow. While no graphene growth was observed, future work will investigate the hypothesized transition region.

Acknowledgements:

Special thanks to Prof. Eric M. Vogel, Christopher Perini and Brian Beatty for guiding me throughout the project. Also, thanks go out to the Georgia Institute of Technology staff, including Dr. Nancy Healy, Joyce Palmer and Leslie O’Neill for their efforts and assistance. Finally, I would like to acknowledge the NSF (under Grant No. ECCS-0335765), the National Nanotechnology Infrastructure Network International Research Experience for Graduates (NNIN iREG) Program, and NIMS.

References:

- [1] A. C. Ferrari, et al., *Nanoscale* 7 (2015) 4598.
- [2] T. Yamada, et al., *J. Phys. D: Appl. Phys.* 46 (2013) 063001.
- [3] D. A. Boyd, et al., *Nature Communications*, 6 (2015).6620.
- [4] Zhang, et al., *ACS Nano*, 6 (2012) 126-132.

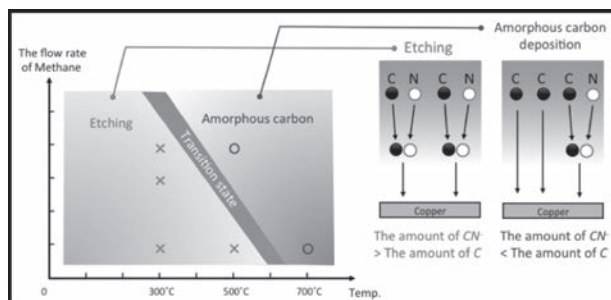


Figure 3: The plot of growth condition and the characteristics of deposited carbon.

Nanofabrication and Characterization of Quasicrystal Metasurfaces using Shadow-Sphere Lithography

Emily MacDonald

Physics, Whitworth University

NNIN REU Site: Center for Nanoscale Systems, Harvard University, Cambridge, MA

NNIN REU Principal Investigator: Prof. George M. Whitesides, Chemistry and Chemical Biology, Harvard University

NNIN REU Mentors: Alex Nemiroski and Mathieu Gonidec, Chemistry and Chemical Biology, Harvard University

Contact: emacdonald16@my.whitworth.edu, gwhitesides@gmwhgroup.harvard.edu, alex.nemiroski@gmail.com

Abstract:

The fabrication and screening processes of quasicrystalline metasurfaces have been optimized to reduce the time and the cost using shadow-sphere lithography (SSL) and template-directed self-assembly. Characterization of these quasicrystals has revealed sharp peaks in reflectance, as well as features as small as 20 nm. The parallel configuration of these quasicrystals allows for hundreds to be fabricated and characterized within hours — much faster than they could be simulated.

Introduction:

Aperiodic and quasiperiodic metasurfaces have great potential for application to ultrasensitive biosensing, but their development has been slowed by difficulties in: i) fabricating them over large areas, and ii) simulating their optical properties computationally. To address these challenges in nanophotonics, the Whitesides lab has recently developed a method for high-throughput fabrication and screening of quasicrystalline metasurfaces using template-directed self-assembly combined with shadow-sphere lithography (SSL). In this project, we focused on optimization of the self-assembly process and on the quasicrystal fabrication and characterization. The speed, versatility of the patterns, and reproducibility of the fabrication process allow for a remarkably quicker and cheaper method for fabrication.

Method:

Templated Self-Assembly. Templated self-assembly reduces the time of fabrication from weeks for a single to a few hours for hundreds. The silicon template was created by first direct writing a pattern into a mask. The image on the mask was a 6×13 array of different quasicrystals, with changing incremental spacing between the holes and different rotational orientations. This image, a single 3.5×7 mm rectangle, was then projected five times smaller using an i-line stepper onto a 76.2 cm photoresist-covered silicon wafer 77 times, until the wafer was covered. The spheres were assembled into the holes of the wafer and then transferred to a glass slide using PDMS. This process is more clearly laid out in Figure 1.

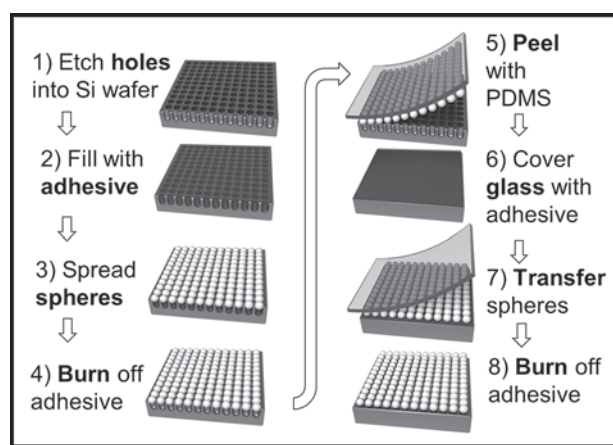


Figure 1: Diagram of the templated self-assembly process [1]. This template shows an arbitrary square pattern.

The spheres retain the pattern initially etched into the silicon. The template is then reusable 10-20 times, allowing for thousands of quasicrystals to be created using a single wafer.

Shadow-Sphere Lithography. Shadow-sphere lithography (SSL) combines techniques from shadow lithography and nanosphere lithography, optimizing both to obtain the finest features. To fabricate, the substrate was placed on a custom-made stage at anywhere between a 45° - 70° angle to the horizontal inside an electron-beam evaporator. Using electron beam physical vapor deposition (EBPVD), a thin film of titanium and then gold was deposited onto

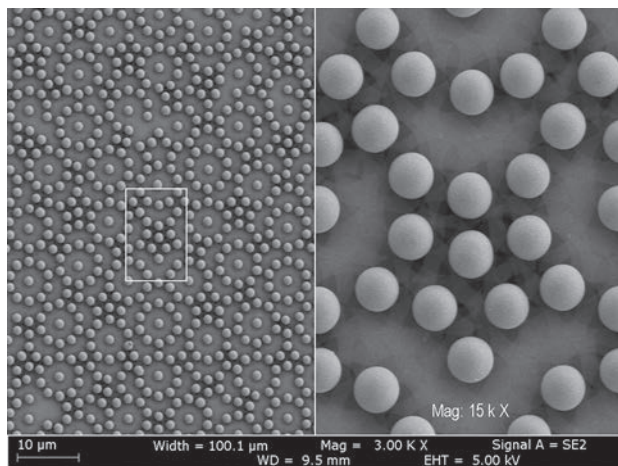


Figure 2: Spheres assembled in a Penrose tiling pattern on the left. On the right is a 5× magnified image of one of the central features with the shadow patterns in between.

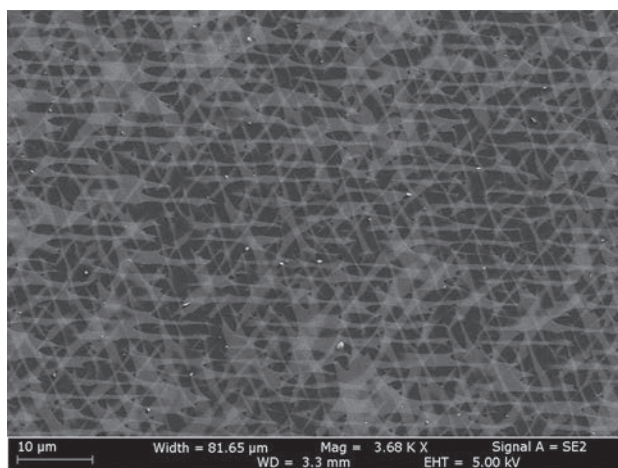


Figure 3: The shadow patterns after the spheres have been removed of a Penrose tiling pattern. The lighter gray is the deposited gold with features smaller than 100 nm.

the stage, which was suspended upside down inside the vacuum chamber. The sample was then rotated while maintaining the original tilt from the horizontal for each deposition of titanium, and then repeated for gold. The spheres were then removed using a simple piece of tape, leaving the shadow patterns — the places where the spheres blocked — behind. Figure 2 shows the spheres and the shadow patterns between them. Figure 3 shows the shadow patterns after the spheres have been removed.

Results:

Using scanning electron microscopy (SEM), it was possible to measure the width of the features on the metasurfaces. Each sample was also characterized using Fourier transform infrared spectroscopy (FTIR). Ideally, the thinner the lines, the sharper the peak in reflectance at certain mid-IR wavelength values. The desired result for sharp peaks was obtained as can be seen in Figure 4,

although not as sharply defined as expected. The difference in spacing led to a sharper peak for the patterns with more densely packed spheres, where the shadow patterns were finer.

Conclusions and Future Work:

We provided proof-of-concept for the fabrication of metasurfaces. Templated self-assembly is possible and allows for a rapid, low-cost method of patterning spheres for the fabrication of quasicrystals, with minimal defects. Mechanizing this process could lead to an almost 100% transfer rate of the spheres. Shadow-sphere lithography creates fine features with replicable accuracy and allows for quasicrystals to be created in parallel. This drastically decreases the time and money required to fabricate and characterize these metasurfaces. Trends can be seen in changing the spacing of the spheres and the rotational orientation in an array of quasicrystals; however, more in-depth analysis needs to be conducted.

Acknowledgements:

Special thanks to my Principal Investigator, George M. Whitesides, and to my mentors Alex Nemiroski and Mathieu Gonidec, as well as to Baris Unal and the staff of Harvard University's Center for Nanoscale Systems. Funding was provided by the NNIN REU Program and the NSF with grant NSF ECCS-0335765.

References:

- [1] Nemiroski, A., et al., Engineering shadows to fabricate optical metasurfaces, *ACS Nano*, 8(11): 11061-70, 2014.

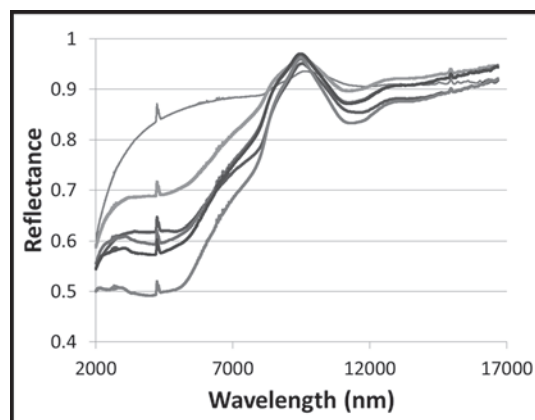


Figure 4: Graph of reflectance from an FTIR scan from 2-17 μm of one column, as spacing increases. The highest line is the background reflectance of the substrate. The lowest line belongs to the most densely packed pattern of spheres. A sharp peak is visible around 10 μm .

Improved Sputtering Conditions for *in situ* Crystallization of PZT Thin Films

Travis O'Neil

Chemical Engineering, Clarkson University

NNIN REU Site: Penn State Nanofabrication Laboratory, The Pennsylvania State University, University Park, PA

NNIN REU Principal Investigator: Dr. Susan Trolter-McKinstry, Materials Science and Engineering, The Pennsylvania State University

NNIN REU Mentor: Hong Goo Yeo, Materials Science and Engineering, The Pennsylvania State University

Contact: oneiltm@clarkson.edu, set1@psu.edu, hxy162@psu.edu

Abstract:

The applications of piezoelectric microelectromechanical systems based on $\text{Pb}(\text{Zr}_x\text{Ti}_{1-x})\text{O}_3$, or PZT, thin films could be expanded by the use of flexible metal foil substrates. Strongly oriented $\langle 001 \rangle$ PZT thin films showing high piezoelectric response with a low dielectric constant have been grown on flexible nickel foil substrates by chemical solution deposition (CSD), which improved the figure of merit for piezoelectric energy harvesters [1]. The goal of this research was to develop a process for growing comparable films by high temperature sputtering, thereby simplifying the deposition process for obtaining desired film thickness with high density and allowing for *in situ* crystallization.

Introduction:

Lead zirconate titanate ($\text{Pb}(\text{Zr}_x\text{Ti}_{1-x})\text{O}_3$, or PZT) has been used for various applications including transducers, sensors, actuators [2] and energy harvesters. Typically, research on these thin films involves platinized silicon substrates. Using flexible metal substrates, such as nickel foil, could vastly improve the uses of PZT thin films due to the improved mechanical durability and flexibility of the metal foil, and because the foil does not mechanically constrain the PZT layer as much as a rigid substrate.

Growth of films greater than $\sim 0.2 \mu\text{m}$ by CSD requires that the spin deposition-pyrolysis-crystallization process be run multiple times. Developing a process for sputtering PZT onto flexible metal substrates would allow for just one deposition step to be done using *in situ* crystallization, thereby eliminating potential drawbacks caused by CSD.

In this experiment, PZT was sputtered onto platinum/titanium/silicon dioxide/silicon substrates with and without a PZT seed layer. This substrate was used because the passivated nickel (Ni) foil requires additional processing steps. Controlling both chamber pressure and oxygen flow during the deposition alters the lead content of the deposited film, which is vital for obtaining pure perovskite PZT without the presence of the non-piezoelectric pyrochlore phase. Temperature was also adjusted to determine the *in situ* crystallization temperature for perovskite PZT.

Experimental Procedure:

PZT thin films were deposited by radio-frequency (RF) magnetron sputtering. The target used for the process

was $\text{Pb}(\text{Zr}_{0.52}\text{Ti}_{0.48})\text{O}_3$, or PZT (52/48), with 10 mole percent excess lead oxide. Additional PbO compensated for loss due to evaporation and/or resputtering, since the sputtering occurred at elevated temperatures and PbO is easily volatilized.

Before the deposition started, the substrates were first gradually heated up and stabilized at a desired temperature. The heating dwell time for the samples in this experiment was set at 90 minutes.

After that, the deposition was run for 15,000 seconds at 90 watts RF power in an argon atmosphere, under varying conditions of temperature, chamber pressure, and oxygen flow. The conditions were optimized sequentially based on the results of previously sputtered samples. Films were sputtered onto the non-seeded and the seeded PZT substrates at the same time. Half of each sample was then rapidly thermal annealed (RTA) at 700°C in O_2 to check for phase and microstructure changes.

X-ray diffraction (XRD) patterns, microstructure images taken by field-emission scanning electron microscopy, and electrical characterization (low field dielectric constant and polarization hysteresis data) were obtained to analyze each sample.

Results and Conclusions:

For the first series of experiments, the chamber Ar pressure was increased. At higher chamber pressures, the bombardment of the growing films is reduced. This, in turn, reduces the presence of the pyrochlore phase. The set temperature was also adjusted in the range of $600\text{--}700^\circ\text{C}$.

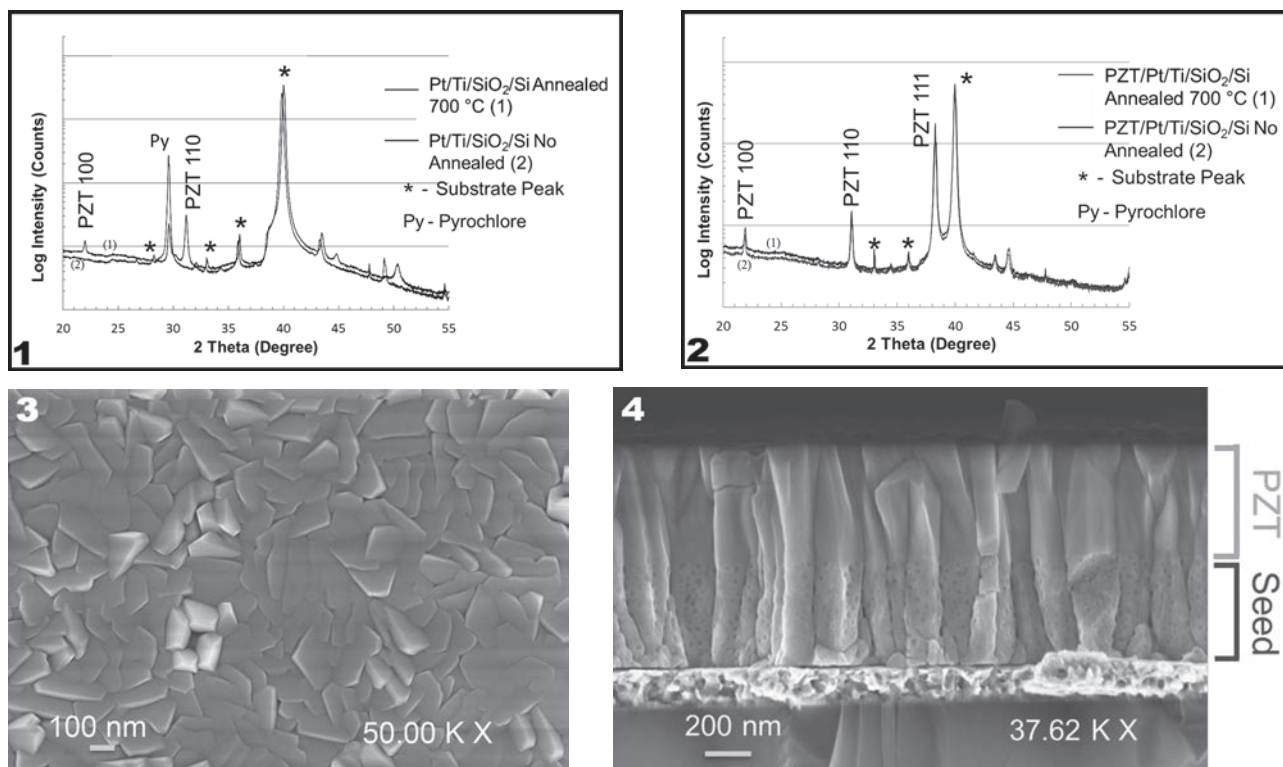


Figure 1, top left: XRD pattern of PZT films without seed layer sputtered at 9 mTorr, 670°C, with 3% oxygen flow. **Figure 2, top right:** XRD pattern of PZT films with seed layer sputtered at 9 mTorr, 670°C, with 3% oxygen flow. **Figure 3, below left:** Top view field-emission scanning electron microscopy (FESEM) image of non-annealed sample with seed layer sputtered at 9 mTorr, 670°C, with 3% oxygen flow. **Figure 4, below right:** Cross section FESEM of non-annealed sample with seed layer sputtered at 9 mTorr, 670°C, with 3% oxygen flow.

It was found that changing only the Ar pressure did not lead to phase-pure perovskite films. Without oxygen flow during sputtering, the best sample was grown at 12 millitorr and 670°C. However, the non-seeded sample showed pyrochlore and the seeded sample showed low intensity perovskite peaks. The seeded sample did show saturated polarization hysteresis loops. These experiments indicated that 670°C was around the crystallization temperature. Neither the XRD perovskite peak intensity nor the microstructure for samples sputtered at this temperature showed much change after annealing.

It has been shown that introducing oxygen into the sputter gas can help initiate perovskite growth on Pt/Ti/SiO₂/Si [3]. In addition, increasing the ratio of oxygen to argon in the sputter gas decreases the lead content of the deposited film [4]. For the next series of experiments, samples were sputtered at 670°C with either 3 or 5% oxygen flow rate in the sputter gas, at different set pressures. It was found that having 3% oxygen flow in the sputter gas, as opposed to 5%, better reduced the pyrochlore present on the XRD patterns. The best sputter conditions of 670°C, 9 mTorr with 3% oxygen flow resulted in an intense pyrochlore peak for the non-seeded sample (Figure 1), yet very intense perovskite peaks for the seeded sample (Figure 2). Samples sputtered under these conditions but with lower pressure showed decreased perovskite crystallinity and increased pyrochlore. It was also shown that sputtering at higher temperatures led to dense films, as seen in Figures 3 and 4.

Moving Forward:

In future work, electrical characterization is needed for films grown at a 9 mTorr chamber pressure at 670°C with 3% oxygen in the sputter gas. It is likely that final optimization will be done by iterative experiments based on structural and electrical characterization. After optimum conditions are found, Ni foil substrates will be used.

Acknowledgements:

I would like to thank my principal investigator Dr. Susan Trolier-McKinstry, mentor Hong Goo Yeo, Kathy Gehoski, and the entire Penn State Nanofab staff for their help throughout this project. This research was supported by the NNIN REU Program and the National Science Foundation under grant no. ECCS-0335765.

References:

- [1] Yeo, H., Trolier-McKinstry, S. (2014). J. Appl. Phys 116. 014105-014105.
- [2] "Physical Basis." Morgan Technical Ceramics. Web. 25 July 2015. <http://www.morgantechnicalceramics.com/sites/default/files/documents/chapter2_1.pdf>.
- [3] Velu, G., et al. (n.d.). Vacuum 56, 199-204.
- [4] Komaki, K., et al. (1994). Jpn. J. Appl. Phys 33, 443-446.

Delta-Doping of Diamond

Stephanie Pastor

Aerospace and Mechanical Engineering, University of Florida

NNIN REU Site: Howard Nanoscale Science and Engineering Facility, Howard University, Washington, DC

NNIN REU Principal Investigator: Dr. Gary Harris, Electrical and Computer Engineering, Howard University

NNIN REU Mentor: Mr. James Griffin, Electrical Engineering, Howard University

Contact: snpastor5@hotmail.com, gharris1124@gmail.com, jagriffin@howard.edu

Abstract:

The nitrogen-vacancy (NV) center in diamond has emerged as a possible versatile tool for data storage in quantum information processing. The NV center consists of a substitutional nitrogen atom located adjacent to a naturally occurring vacancy within the diamond lattice. The spins of the unbound electrons within the bond can be coherently controlled at room temperature and read out optically. The focus of this project was to determine the optimal conditions for NV center production in synthetic, polycrystalline diamond by growing and doping with ^{15}N gas in a hot filament chemical vapor deposition (HFCVD) reactor. The nitrogen isotope allowed us to distinguish our deposited nitrogen atoms from other impurities, such as ^{14}N or silicon atoms, that may also be present within the grown diamond.

Introduction:

Quantum computers are considered to be the next revolution in data processing because they will have much faster computing power than modern-day computers. Quantum bits (qubits), the basic unit for quantum information, are formed by electron spins that can be controlled and manipulated to store and read out data. The NV center will allow us to implement logic in the form of these qubits.

Experimental Procedure:

Silicon (Si) and silicon carbide (SiC) samples were cleaned by sonication in acetone and then methanol for one minute each. Nanodiamonds, approximately 5 nm diamond seeds used to increase nucleation density, were deposited by sonicating the samples in an equal volume mixture of

nanodiamond solution and methanol for 10 minutes, then rinsing in methanol.

The diamond films were grown in an HFCVD reactor. As seen in Figure 1, the introduction of hydrogen (H_2) and methane (CH_4) gases into the hot filament zone causes decomposition of the gases into simpler molecules and atoms. Atomic hydrogen helps to further decompose the hydrocarbon species at and above the heated substrate surface, leaving behind only carbon atoms for diamond and/or graphitic growth. The atomic hydrogen was also used to etch any graphitic material formed during the growth process.

During the diamond growth process, the flow rate of hydrogen and methane were maintained at 80 sccm and 1 sccm respectively. The chamber pressure and substrate

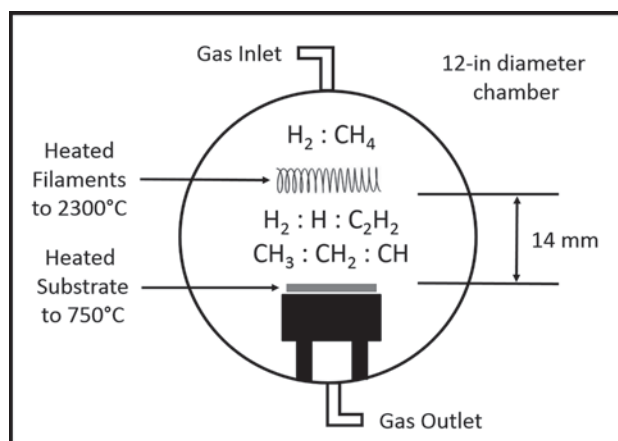


Figure 1: Diagram of HFCVD growing chamber.

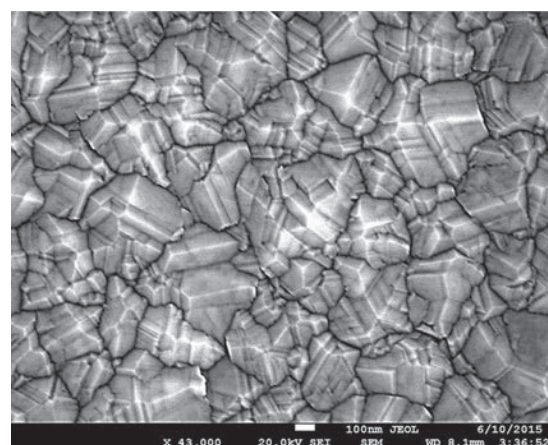


Figure 2: SEM image of diamond grown on Si.

temperature were maintained at 20 torr and 750°C respectively. These conditions yielded a diamond growth rate of 0.167 $\mu\text{m}/\text{hour}$ at a substrate-to-filament gap of 14 mm. Figure 2 shows a scanning electron microscope (SEM) image of diamond grown on Si after this process.

Delta doping of diamond with ^{15}N gas was performed during diamond growth at the surface or a few nanometers below the surface. In one experiment, the ^{15}N gas flow rate was varied from 4 to 12 sccm while growing on both Si and SiC substrates with a substrate-to-filament gap of 14 mm. The goal of this experiment was to determine how NV center concentration varied with ^{15}N gas flow rates.

In a second experiment, the ^{15}N gas flow rate was varied from 2 to 12 sccm with a substrate-to-filament gap reduced to 7 mm. The goal of this experiment was to see if NV center concentration varied with substrate-to-filament gap. Since the mean-free path of atomic nitrogen is finite, reducing the distance the atomic nitrogen has to travel before incorporation in the diamond lattice may increase NV center production.

Results:

Figure 3 shows a typical Raman spectrum of HFCVD diamond grown throughout this work. This particular sample was grown on silicon and the diamond was

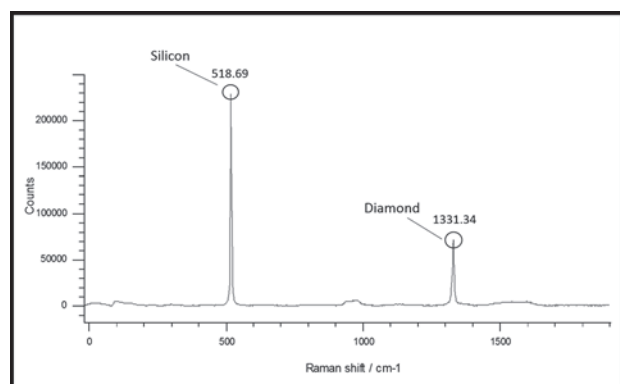


Figure 3: Raman data of undoped diamond on Si.

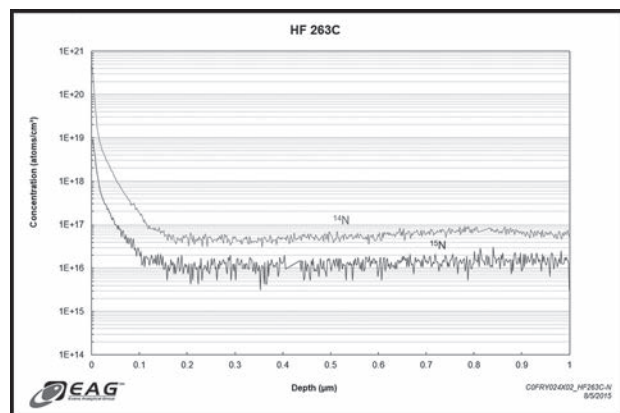


Figure 4: SIMS data indicating nitrogen concentration of a doped diamond on Si sample.

undoped with an average roughness of 40 nm. The sharp diamond peak at 1331.34 cm^{-1} with a FWHM of 7.6 cm^{-1} is indicative of high quality diamond. All of the diamond films grown by the seeding process are polycrystalline. Because the equipment necessary for NV center detection was not available locally, the samples were sent out for characterization. Unfortunately the tool that was used did not detect any NV centers in the samples. This was believed to be an equipment malfunction and not an absence of NV centers. Previous experiments using the same tool indicated NV center presence with a 637 nm zero-phonon emission on ^{14}N doped HFCVD diamond.

Secondary ion mass spectrometry (SIMS) analysis of one surface delta doped diamond sample was obtained, see Figure 4. This plot shows the concentration of ^{14}N and ^{15}N atoms as a function of depth from the surface. At the surface it is clear that both ^{14}N and ^{15}N were incorporated in the diamond film at very high concentrations, with ^{14}N reaching over 10^{20} atoms/ cm^3 and ^{15}N reaching about 10^{19} atoms/ cm^3 .

Conclusions:

High quality diamond was grown on Si and SiC substrates by HFCVD. The fact that the diamond films were polycrystalline may or may not prove detrimental for NV center purposes. However, growth of diamond on diamond substrates is desirable due primarily to a much smoother surface. SIMS data indicated a delta doped behavior of both ^{14}N and ^{15}N in diamond films. Unfortunately, determination of how ^{15}N gas flow rates and filament-to-sample gaps affect NV center production is still unknown for this reactor. However, in previous experiments involving the doping of diamond with ^{14}N gas, NV centers were characterized and produced under similar parameters. Therefore, it is reasonable to conclude that NV centers exist in diamond films doped with ^{15}N gas.

Acknowledgements:

I would like to thank the following individuals and organizations for their support: Dr. Gary Harris, Mr. James Griffin, the Howard Nanoscale Science and Engineering Facility at Howard University, the Laboratory for Nanoscale Optics at Harvard University, the National Nanotechnology Infrastructure Network International Research Experience for Undergraduates (NNIN iREU) Program and the National Science Foundation, Grant No. ECCS-0335765.

References:

- [1] May, P.; CVD Diamond - a New Technology for the Future?; Endeavour, Volume 19, Issue 3, Pages 101-106, 1995.
- [2] Wöhrle, N. (Director) (2014, December 30). Diamonds Are a Quantum Computer's Best Friend. 31st Chaos Communication Congress of the Chaos Computer Club. Lecture conducted from, Hamburg.

Diverse Patterns and Geometries in Self-Assembled Block Copolymer Thin Films Through Multilayer Mixing

Christopher Phenicie

Physics, University of Minnesota-Twin Cities

NNIN REU Site: Colorado Nanofabrication Laboratory, University of Colorado, Boulder, CO

NNIN REU Principal Investigator: Mark P. Stoykovich, Chemical and Biological Engineering, University of Colorado, Boulder

NNIN REU Mentor: Garrett Chado, Chemical and Biological Engineering, University of Colorado, Boulder

Contact: phenic004@umn.edu, mark.stoykovich@colorado.edu, garrett.chado@colorado.edu

Abstract:

Lithography via the self-assembly of block copolymers is a promising tool for nanostructure fabrication on the order of 10 nm. Once assembled, one block of the copolymer can be selectively removed and metal can be deposited on the remaining pattern. This can be used to create structures such as metal nanodots and highly connected metal nanowire networks with varying periodicities. The morphology of the block copolymer self-assembly is dependent on the volume fraction of each block in the copolymer. A technique called multilayer mixing is presented, whereby we are able to change the morphology of block copolymer after the block copolymer has self-assembled, by increasing the volume fraction of one of the blocks. This is accomplished through spin casting a layer of homopolymer on top of it and solvent annealing the sample to let it reach the equilibrium morphology.

Introduction:

Block copolymers (BCPs) are a class of macromolecules consisting of two chemically distinct, covalently bonded polymer chains. The BCP phase separates into regular patterns with structures on the order of 10 nm. These features have long range ordering, consistent across chips at least one square centimeter in size. The patterns formed through BCP self-assembly is dependent on the volume fraction of each block in BCP.

Materials and Methods:

A substrate with neutral preference for each block of the BCP was prepared by coating a silicon wafer with the random copolymer poly(styrene-*r*-methyl methacrylate-*r*-glycidyl methacrylate) $P(S_{0.58}\text{-}r\text{-}MMA_{0.41}\text{-}r\text{-}GMA_{0.01})$ brush layer, where the subscripts indicate the mole fraction of each monomer. Silicon wafers were purchased from Montco Silicon and rinsed with DI water, acetone, and toluene via spin casting prior to depositing the brush layer. The neutral substrate was then thermally annealed at 190°C for 60 min under vacuum, followed by sonication in toluene for 5 min and spin coating in toluene for 30 s at 5000 rpm.

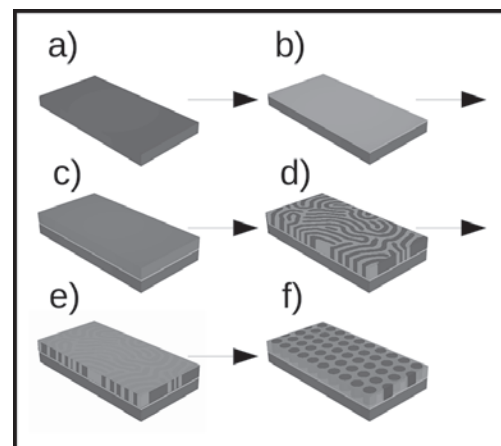


Figure 1: (a) All block copolymer is deposited on a silicon substrate (b), which is functionalized with a brush layer of PS-*r*-ePMMA. (c) Then, lamellar BCP is deposited on the brush via spin casting. (d) The block copolymer is then solvent annealed to form lamellae. (e) After annealing, PMMA homopolymer is deposited on top of the lamellae via spin casting and (f) the sample is solvent annealed once again, allowing the PMMA to mix with the lamellae ("multilayer mixing") to form cylinders.

Lamellar forming poly(styrene-*b*-(methyl methacrylate-*r*-glycidyl methacrylate), PS-*b*-(PMMA-*r*-GMA), was synthesized by sequential atom transfer radical polymerization of styrene (Sigma-Aldrich, 99%), methyl methacrylate (Acros, 99%), and glycidyl methacrylate (MP Biomedicals, 99%) as reported elsewhere [1]. All BCP samples were deposited via spin casting at 5000 rpm for 30 s. The BCPs were self-assembled through solvent vapor annealing in an even mixture of acetone and cyclohexane for 4 hr. The solvents were degassed in a 25 mTorr vacuum to remove any dissolved gases prior to solvent annealing.

Multilayer mixing was achieved by depositing a layer of PMMA homopolymer on the lamellar BCP after annealing. The PMMA homopolymer used for the multilayer mixing was purchased from Polymer Source (M.W. = 21.2 kg mol⁻¹, PDI = 1.07). Prior to deposition of this PMMA homopolymer, BCP samples were baked at 90°C for

30 min. The PMMA homopolymer was deposited via spin casting at 5000 rpm for 30 s. Samples were solvent annealed in the same conditions as the first solvent anneal. Samples were etched to improve image clarity (RIE, 160 mTorr oxygen plasma, 55W, 5 s).

Discussion:

Multilayer mixing was achieved as shown schematically in Figure 1. In essence, the method allowed the equilibrium morphology of the BCP to be changed, from lamellae to cylinders, through the addition of PMMA homopolymer. As shown in Figure 2, the addition of PMMA homopolymer increased the volume fraction of PMMA in the thin film, inducing a phase transition from the lamellar to the cylindrical morphology. A BCP that is 77% PMMA has an equilibrium morphology of hexagonally packed cylinders. This shows that multilayer mixing is capable of transitioning one equilibrium BCP morphology to a distinct equilibrium morphology.

However, for the samples with less than 77% PMMA, notice in Figure 2 that the cylinders tended to follow the lamellae rather than have hexagonal packing. This suggests that the mechanism of multilayer mixing involves lamellae breaking up into cylinders. This was further substantiated by annealing BCP with 77% PMMA for less than 4 hr, as shown in Figure 3. With less annealing time, the samples did not have enough time to reach their equilibrium morphology of hexagonally packed cylinders. These images then show how the process of solvent annealing evolved over time. Figure 3 suggests that, in this process, cylinders first formed following the previously existing lamellae and then reorganized to achieve hexagonal packing. If so, the spacing of cylinders can be controlled by first directing the assembly of lamellae before the multilayer mixing.

Conclusions:

It has been shown that it is possible to control the self-assembled patterns of block copolymers via the technique of multilayer mixing. This has applications, for instance, to computer memory devices, allowing the creation of smaller nanodots and nanowires for computer chips. Future research could include directing the assembly of lamellae to guide cylinder formation.

Acknowledgements:

This research was supported by the National Science Foundation under Grant No. ECCS-0335765. The author would like to thank CNL and NCF staff for help with sample preparation and characterization, and NNIN staff for organizing this National Nanotechnology Infrastructure Network Research Experience for Undergraduates (NNIN REU) Program.

References:

- [1] He, C. et al., Small, 2015 DOI: 10.1002/sml.201403364.

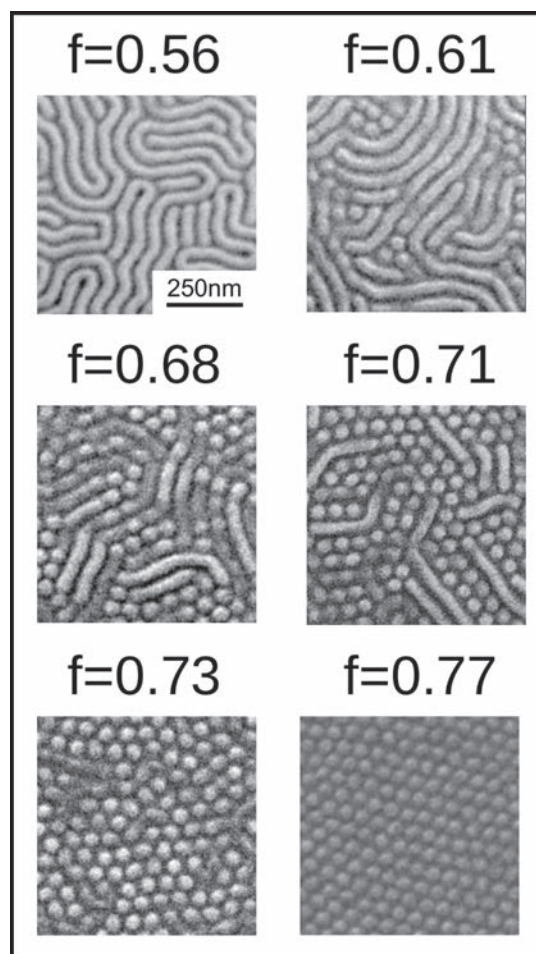


Figure 2: SEM images of BCP morphology after multilayer mixing with varying volume fraction of PMMA. A second layer of varying concentration of PMMA (M.W. = 21.2 kg mol⁻¹) was spin cast and allowed to mix with the BCP layer under solvent vapor for 4 hours to create samples with varying volume fraction of PMMA (f).

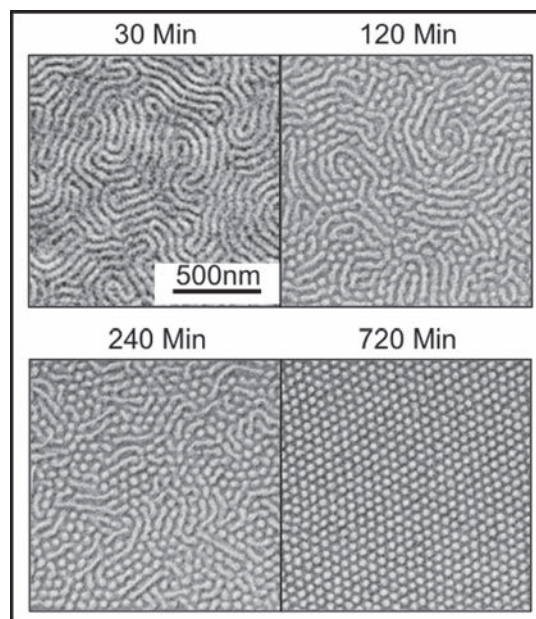


Figure 3: SEMs of cylinders created from multilayer mixing with PMMA annealed at varying times. Each image is a snapshot of the annealing process as a function of time.

Synthesis and Characterization of Size- and Shape-Specific Gold Nanocrystals for Superlattice Assembly

Elyse Pizzella

Chemical Engineering, North Carolina State University

NNIN REU Site: Washington Nanofabrication Facility and Molecular Analysis Facility, University of Washington, Seattle, WA

NNIN REU Principal Investigator: Vincent Holmberg, Chemical Engineering, University of Washington

NNIN REU Mentors: Soohyung Lee and Elena Pandres, Chemical Engineering, University of Washington

Contact: ecpizzel@ncsu.edu, holmvc@uw.edu, shlee16@uw.edu, epandres@uw.edu

Abstract:

In this work, gold nanoparticles of different shapes and sizes were systematically synthesized, characterized, and assembled. The best control over their size distribution and morphology was achieved using seed-mediated growth. By varying reaction and sample preparation conditions, gold nanocrystal (AuNC) growth was directed into various shapes. These nanocrystals were characterized using UV-vis spectroscopy, scanning electron microscopy (SEM), and transmission electron microscopy (TEM) to determine final shapes and packing structures. The amount of free ligand in solution and the concentration of seeds used in the growth solution resulted in visible differences in both nanocrystal morphology and their packing assemblies. Sample preparation conditions, including drying temperature, drying speed, and droplet orientation, were also investigated. By successfully controlling reaction parameters and sample preparation conditions, it is possible to synthesize uniform, ordered structures with tailored shape- and size-specific properties.

Introduction:

Colloidal AuNCs have many applications in optical [2] and medical sensing, and when assembled into collective structures, their properties are even further tunable. In this work, AuNCs were synthesized and assembled into close-packed structures.

Experimental Procedure:

Size- and shape-specific gold nanocrystals were fabricated using seed-mediated growth [4], which involved making aqueous seed solutions and growth solutions separately. By exploring parameters involved in synthesis and preparation, we hoped to achieve ordered, close-packed structures of AuNCs by producing crystals with monodisperse shape and size.

Seed Solution Preparation. A 10 mL aqueous solution of 2.5×10^{-4} M hydrogen tetrachloroaurate trihydrate (HAuCl_4) and 0.10 M cetyltrimethylammonium chloride (CTAC) was prepared. Next, a cold, 10 mL aqueous solution of sodium borohydride (NaBH_4) was prepared. When ready, 45 μL of the NaBH_4 solution was added to the HAuCl_4 solution and allowed to stir for two minutes to initiate nucleation of AuNC seeds. The solution was then aged for at least one hour at 30°C.

Growth Solution Preparation. Multiple aqueous growth solutions were prepared (10 mL total volume). The synthesis of two shapes of gold nanocrystals (cubes and rhombic dodecahedra) were targeted. To direct the nanocrystal shape, different amounts of ascorbic acid (the shape-directing agent) were added. All reagent volumes

in the growth solutions were kept constant (0.32 g CTAC, 250 μL stock HAuCl_4 , and 10 μL of 0.01 M NaBr solution) except for the water and ascorbic acid. For cubic shapes, 9.625 mL deionized water and 90 μL ascorbic acid were added to the other reagents in the vials; for rhombic dodecahedral shapes, 9.565 mL deionized water and 150 μL ascorbic acid were added.

Directing the AuNC Size. To tune the nanocrystal size, the volume of seed solution added to the growth solutions was varied. For each target shape (cubes and rhombic dodecahedra), three different nanocrystal sizes were prepared by adding 25 μL , 45 μL , and 100 μL of seed solution to the growth solutions.

Purification and Deposition. The final solutions were purified via centrifugation, and droplets of the different solutions were deposited onto silicon wafers. Cleanliness of solution, drying temperature, and evaporation rate all affected the AuNC assembly process and SEM image quality.

Results and Conclusions:

The AuNCs displayed a clear size trend, depending on the volume of seed solution that was added to the growth solution, as shown in Figure 1. As the number of seeds added to the growth solution increased, final nanocrystal size decreased, and vice versa. This is because if larger quantities of seed are added to a growth solution, there is less growth reagent available per seed, resulting in smaller crystals.

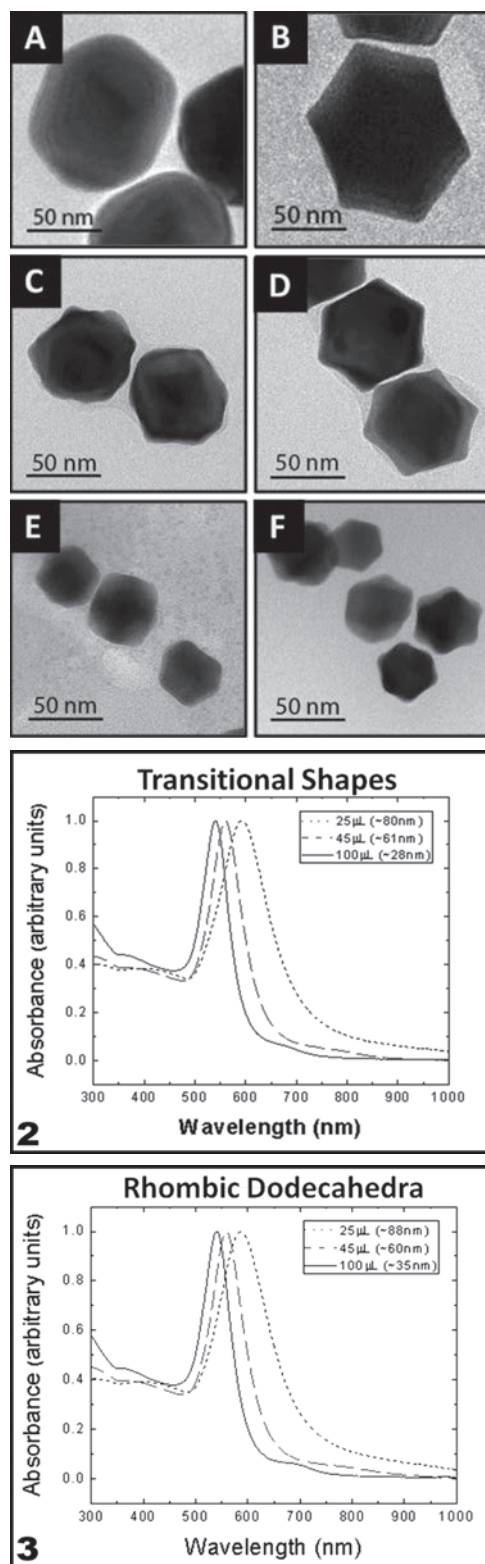


Figure 1, top: AuNCs with different volumes of seed solution added. Left column: Transitional shapes; A) 25 μL , C) 45 μL , E) 100 μL . Right column: Rhombic dodecahedra; B) 25 μL , D) 45 μL , F) 100 μL . **Figure 2, middle:** The largest size AuNC (80 nm) has the plasmon band furthest in the infrared because its electrons oscillate at a longer wavelength than smaller size AuNCs. **Figure 3, bottom:** A similar trend in plasmon frequency is seen here with a red-shift in peak position as the AuNC increases in size.

In Figures 2 and 3, there is shown a clear trend between the optical properties of the AuNCs and their size. Since gold is a plasmonic material, different AuNC diameters resulted in different plasmon bands (the peaks in the graphs). This is because the electrons in the particles oscillated collectively at different frequencies for particles with different dimensions [2].

Although rhombic dodecahedral nanocrystals were synthesized successfully, the cubic shapes that were targeted more closely resembled a transitional shape somewhere between a cube and a rhombic dodecahedron. Figure 4 displays several of the close-packed assemblies that were achieved. It is evident that the size and shape monodispersity of the AuNCs was the most important factor in achieving well-ordered structures.

Future Work:

With greater control over AuNC size and shape, it is possible to assemble them into chains, 2D superlattices, and 3D supercrystals. These structures enable a variety of applications in metamaterials [2], optical sensors, and acoustic wave sensors [1], due to their collective plasmonic properties [3] when assembled into ordered supercrystals.

Acknowledgements:

I would like to thank the NNIN REU Program, as well as the NSF, Grant No. ECCS-0335765, for funding this research opportunity. I would like to also express my deepest gratitude to my mentors, Soohyung Lee and Elena Pandres, and my principal investigator, Vincent Holmberg, for what they taught me over the course of this project.

References:

- [1] Chiu, Chi-Shun, et al. *J. Phys. Chem.*, 117, 2442-2448 (2012).
- [2] Gwo, Shangji, et al. *Langmuir*, 28, 8902-8908 (2012).
- [3] Lin, M.-H, et al. *J. Am. Chem. Soc.*, 132, 11259-11263 (2010).
- [4] Wu, H.-L, et al. *Langmuir*, 26(14), 12307-12313 (2010).

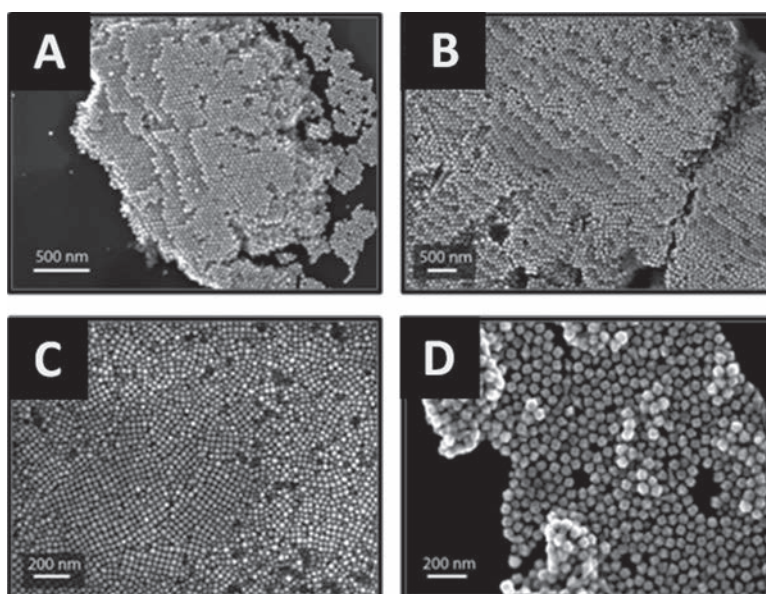


Figure 4: Some of the most closely-packed AuNC structures achieved under various conditions. Well-ordered structures occurred largely because of the monodispersity of the crystals within the sample.

The Optimization of Thin Film Molybdenum Disulfide Synthesis

Michael Statt

Chemical and Biomolecular Engineering, Cornell University

NNIN REU Site: Institute for Electronics and Nanotechnology, Georgia Institute of Technology, Atlanta, GA

NNIN REU Principal Investigator: Prof. Eric Vogel, School of Materials Science and Engineering, Georgia Institute of Technology

NNIN REU Mentors: Philip Campbell and Dr. Alexey Tarasov, School of Materials Science and Engineering, Georgia Institute of Technology

Contact: mjs488@cornell.edu, eric.vogel@mse.gatech.edu, philip.campbell@gatech.edu, alexey.tarasov@mse.gatech.edu

Abstract and Introduction:

Two-dimensional materials have been a source of great interest and promise due to their interesting thickness-dependent properties. One class of these materials are transition metal dichalcogenides (TMDCs). TMDCs are layered materials with formula MX_2 , where M is a transition metal (Mo, W, etc), and X is a chalcogen (S, Se, Te). TMDCs exhibit high mechanical strength and thickness-tunable band gaps that transition to direct band gaps in the monolayer limit for most TMDCs.

Molybdenum disulfide (MoS_2) is one example of a TMDC that has garnered significant interest recently due to its direct band gap at a monolayer thickness, high on/off ratios, and moderate mobilities. These properties make MoS_2 well-suited for applications such as 2D vertical heterostructure devices, thin film optoelectronics, and flexible, transparent electronics [1].

For TMDCs to be compatible with modern electronic fabrication processes, uniform, high quality, wafer-scale growths must be achieved. One straightforward approach to MoS_2 synthesis is the sulfurization of an evaporated thin film of molybdenum by annealing in a sulfur-containing environment at high temperatures. This method has been shown to create highly uniform, wafer-scale, trilayer MoS_2 films [2]. The resulting films, however, suffer from small grain sizes (~ 10 nm), which increase charge-carrier scattering, limit carrier mobility and reduce on/off ratios. This study investigated the effects of high temperature annealing on the crystallinity of MoS_2 films synthesized through sulfurization of thin molybdenum films.

High temperature annealing has been shown to cause lattice recrystallization and coarsening of the resultant grain structure [3]. Experimental results suggest that extended sulfur-rich and sulfur-deficient anneals are currently incompatible with high quality MoS_2 synthesis.

Experimental Methods:

Silicon wafers were thermally oxidized to form a 300 nm thick layer of SiO_2 . A 1 nm layer of molybdenum was deposited on the SiO_2 using e-beam evaporation. The samples were then placed in a sulfurization furnace and

pumped down to the chamber base pressure (~ 30 mTorr). The samples were annealed at $300^\circ C$ for 30 minutes in an $Ar:H_2$ (4:1) atmosphere to remove atmospheric contaminants. In a separate vessel, a powder sulfur source was concurrently heated to $150^\circ C$ to increase its vapor pressure. The sulfur vapor was injected into the chamber, which was backfilled with argon gas to a total pressure of approximately 5 Torr. The chamber was then heated to $1000^\circ C$ and allowed to dwell at that temperature for times varying from five minutes to 12 hours to allow for sulfur to diffuse into the molybdenum layer and react to form MoS_2 . This step will be referred to as the sulfur anneal step.

Next, the chamber was purged with argon gas at temperatures varying from $750^\circ C$ - $1000^\circ C$ to remove any remaining sulfur gas. This process step required a minimum dwell time of 30 minutes to prevent sulfur precipitation on film surface and was extended up to 12 hours to thermally anneal the sample. This step will be referred to as the argon anneal step. The chamber was then cooled to room temperature under an argon flow.

XPS was used to characterize film stoichiometry and elemental composition. Raman spectroscopy was used to identify MoS_2 film uniformity and thickness through the appearance and separation of characteristic MoS_2 A_{1g} and E_{2g}^1 peaks, which have been shown to be correlated with film thickness [4].

Results and Conclusions:

Sulfur anneal times longer than two hours yielded partially oxidized MoS_2 films, as indicated by the appearance of MoO_2 and MoO_3 peaks in the XPS spectra shown in Figure 1. These films also showed large areas with no characteristic MoS_2 Raman spectroscopy peaks. It was also found that small, ordered, circular regions of anomalous MoS_2 growth occurred in extended sulfur anneal time samples, as shown in Figure 2. These regions grew in size and density when sulfur anneal time was increased. Raman spectroscopy analysis of these regions indicated bulk thickness MoS_2 growth and atomic force microscopy (AFM) analysis showed that these regions were steps

approximately 10-30 nm above the rest of the film. It is currently unknown what caused these bulk thickness regions, but they limited the viability of extended sulfur anneals to increase grain size.

When argon anneal temperatures were kept at 1000°C, argon anneal times longer than two hours yielded samples

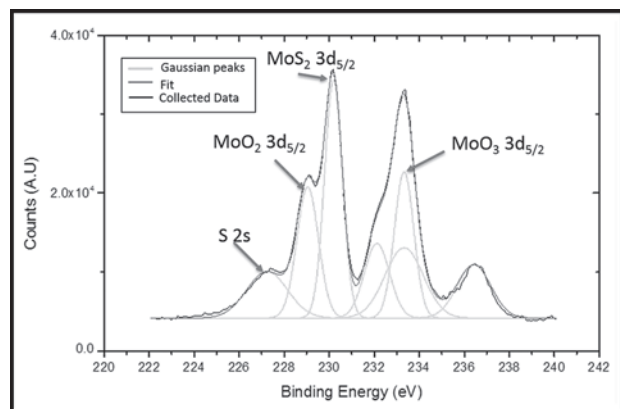


Figure 1: XPS spectra of sample annealed in sulfur-rich environment for 120 minutes.

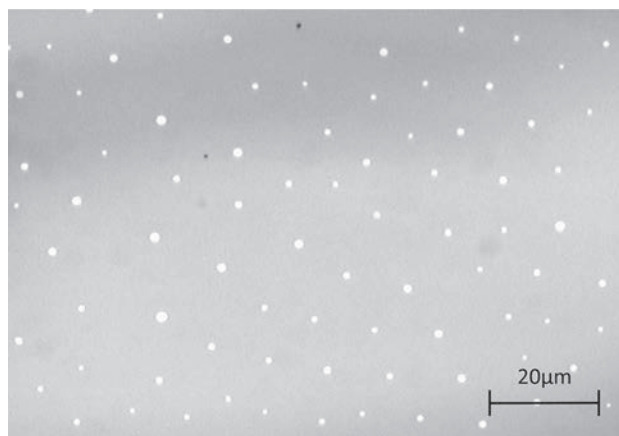


Figure 2: Optical micrograph shows bulk thickness spots on sample grown at 120 minute sulfur anneal time.

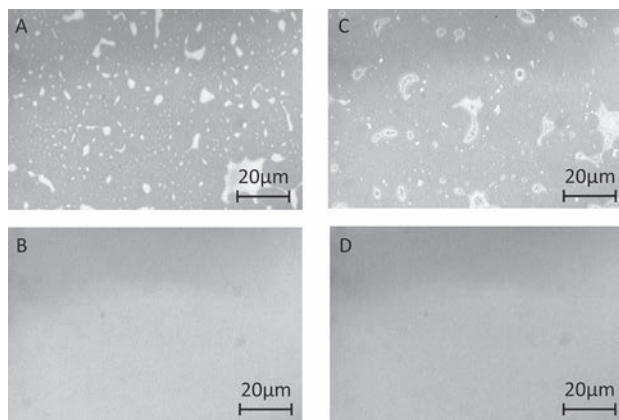


Figure 3: A and B are pre-sulfurization, C and D are post-sulfurization. A and C were cleaned with IPA and acetone, B and D were not.

with little to no sulfur content, as indicated by XPS analysis, and no characteristic MoS₂ peaks in Raman analysis. When temperatures were reduced to 750°C, a two hour argon anneal resulted in MoS₂ peaks in Raman analysis, but peak separation indicated highly varying thickness across the sample (± 3 monolayers). This indicated that sulfur may be evaporating from the MoS₂ film due to a concentration gradient between the film and the sulfur-deficient atmosphere. Currently, this limitation makes extended argon anneals an unviable option for increasing crystallinity in MoS₂ films.

During this investigation it was found that using organic solvents, isopropyl alcohol and acetone, to clean samples caused bulk thickness MoS₂ growth similar to that seen in extended sulfur anneal times. Figure 3 shows this through two samples grown concurrently: one cleaned with organic solvents and one cleaned only with a nitrogen gun. Bulk MoS₂ grew in regions where residue from organic solvents was present, while no MoS₂ grew in regions without residue. This indicates that organic surface contamination on the sample is altering the surface chemistry of the reaction.

Future Work:

These preliminary results indicate that high temperature anneals detrimentally affect MoS₂ film quality. In the future, conditions causing bulk thickness growth during long sulfur anneals must be quantified and mitigated to allow for uniform thickness growths. Transmission electron microscopy (TEM) and low energy electron diffraction (LEED) must be used to image MoS₂ grain structure.

Acknowledgements:

I would like to thank Professor Eric Vogel for this opportunity, the Vogel group for their mentorship; and Joyce Allen, Leslie O'Neill, and Dr. Nancy Healy for their coordination. This research was supported by the National Nanotechnology Infrastructure Network Research Experience for Undergraduates (NNIN REU) Program and NSF (Grant No. ECCS-0335765).

References:

- [1] Wang, Q. H; Nature Nanotechnology; 7(11), 699-712, (2012).
- [2] Tarasov, A; Advanced Functional Materials; 6389-6400 (2014).
- [3] Humphreys, F. J.; Recrystallization and related annealing phenomena, Elsevier; (1995).
- [4] Lee, C.; ACS Nano; 4(5), 2695-2700. (2010).

High Storage Capacity Sodium-Ion Battery Electrodes of Solution-Grown Germanium Nanowires

Yuichi Tsujiura

Mechanical Engineering, Kobe University, Japan

NNIN iREG Site: Microelectronics Research Center, The University of Texas, Austin, TX

NNIN iREG Principal Investigator: Dr. Brian A. Korgel, Chemical Engineering, The University of Texas at Austin

NNIN iREG Mentor: Taizhi Jiang, Chemical Engineering, The University of Texas at Austin

Contact: tsujiura@stu.kobe-u.ac.jp, korgel@che.utexas.edu, tzjiang@utexas.edu

Introduction:

Sodium-ion batteries (NIBs) have attracted attention as an alternative to lithium-ion batteries (LIBs) because sodium (Na) is so much more abundant and inexpensive than lithium (Li). NIBs, however, require much higher performance in order to displace the use of LIBs. One problem is that graphite—the negative electrode material used in LIBs—has no considerable reversible capacity for NIBs [1]. Therefore, NIBs require the development of new electrode materials. Germanium (Ge) is one promising candidate for the negative electrode, with reversible sodiation at room temperature with a relatively high theoretical capacity (NaGe, 369 mAh/g) [2], comparable to graphite for LIBs. In nanowire form, Ge can also tolerate the volume changes that occur during cycling without degradation, and a high surface area-to-volume ratio yields suitable charge/discharge kinetics in the battery.

Ge nanowires (GeNWs) were synthesized by a supercritical-fluid-liquid-solid (SFLS) growth process [3] and three procedures were applied to improve NIB performance. First, GeNWs were activated for sodiation by an initial lithiation cycle that amorphized the nanowires. Kohandehghan, et al., showed that crystalline GeNWs do not sodiate until being activated with Li [4]. Second, the surface of Na foil counter electrodes were polished to remove surface oxide, which greatly enhanced the performance of GeNW half-cells. Third, the role of the thickness of GeNW electrode layer was studied to understand kinetic limitations of the battery.

Experimental Procedure:

GeNWs were produced by the SFLS growth process. A reactant solution containing 25 μL of Au nanocrystal stock solution, 190 μL of DPG, and 85 μL of monophenylesilane (MPS) in toluene was injected into a reactor heated to 380°C and pressurized to 6.2 MPa at a rate of 0.5 mL/min for 40 minutes.

For testing in coin cells, GeNWs were combined with poly(acrylic acid) (PAA) binder and conductive carbon at a weight ratio of 70:20:10 [5]. To obtain a viscous slurry,

the mixture was dispersed in 1-methyl 2-pyrrolidinone (NMP). Then, the slurry was doctor-bladed (50-200 μm gap) onto copper (Cu) foil and vacuum dried at 150°C. Individual 11 mm diameter circular electrodes were hole-punched from the coated Cu foil.

The GeNWs were activated for sodiation by an initial lithiation step. An LIB half-cell was assembled from stainless steel coin cells, GeNW anode, Li foil counter

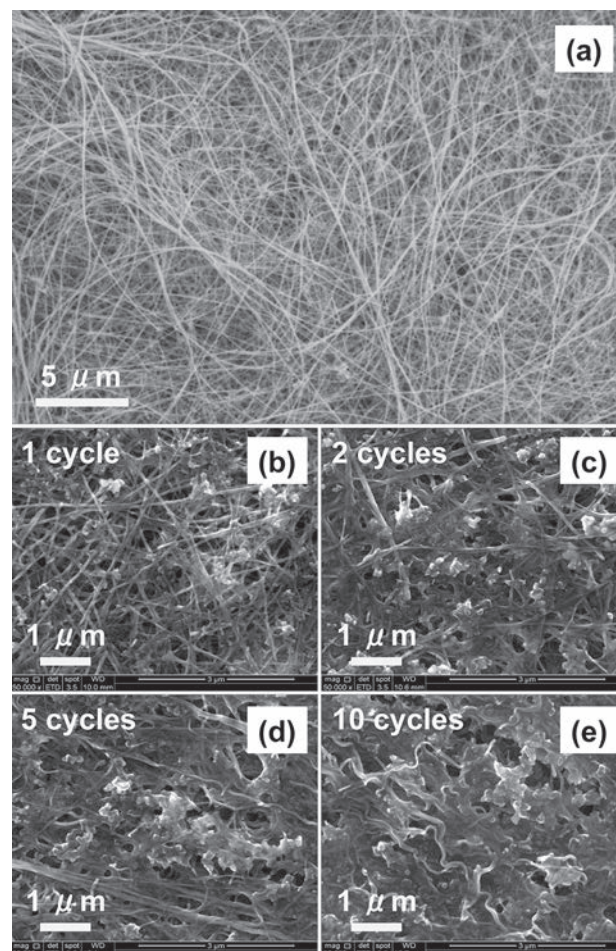


Figure 1: SEM images of (a) as-grown GeNWs and (b)-(e) Li-activated GeNWs with 1, 2, 5, and 10 cycles.

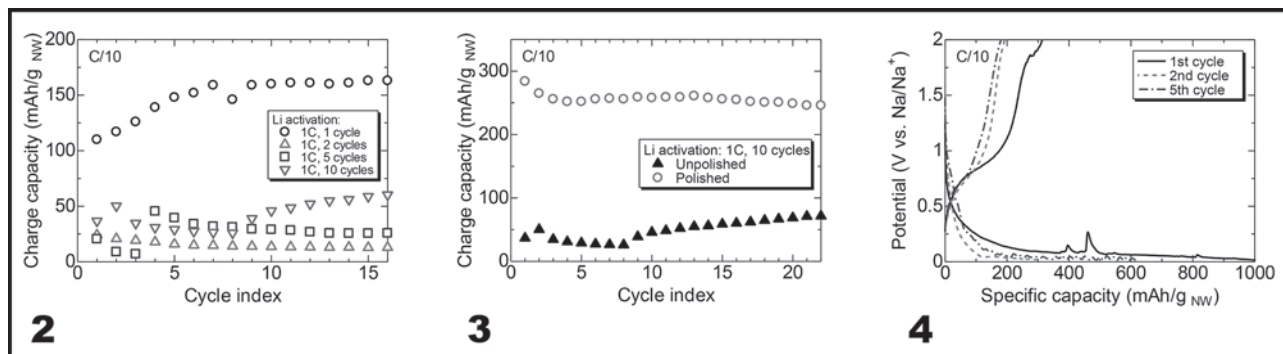


Figure 2, left: The charge capacity of NIBs with Li-activated GeNW anode with each cycle. **Figure 3, middle:** The charge capacity of NIBs with polished and unpolished Na foil counter electrode. **Figure 4, right:** The voltage profile of NIB with GeNW electrode film thickness of 1.0 μm .

electrode, a few drops of electrolyte, and separator. After charging and discharging with Li for one cycle at a rate of 1C, the LIB is disassembled. The GeNW anode is then reassembled into a half-cell with a Na foil counter electrode. The NIB was tested at a rate of C/10.

Results and Conclusions:

Figures 1(a) and (b)-(e) show SEM images of the GeNWs before and after cycling against Li. In Figures 1(b)-(e), the SEM images show that the solid electrolyte interphase (SEI) layer increased in thickness with each lithiation cycle. Figure 2 shows the cycle performance of NIBs made with GeNWs activated with Li with a different number of cycles. The highest charge capacity in the NIB was obtained with a single lithiation/delithiation activation cycle. Based on the SEM data, it appears that thicker SEI layers formed during the Li activation step hampers NIB performance and should be limited as much as possible.

Figure 3 shows NIB data for GeNW coin cells made with polished and unpolished Na foils. The polished Na foil counter electrode led to charge capacities that were three times higher than the NIBs made with unpolished electrodes. To improve reversibility, the effect of GeNW electrode film thickness was studied. Figure 4 shows the voltage profile of the NIB with a GeNW layer thickness of 1.0 μm . A charge capacity of more than 300 mAh/g was obtained. Changes in the layer thickness from 0.7 μm to 1.3 μm did not affect the battery performance. This electrode layer thickness probably represents a rate-limiting thickness.

Future Work:

Future work will involve the synthesis of tin (Sn)-coated GeNWs to enhance reversibility and rate capability in

the electrode. The influence of thinner electrode layers on the NIB rate capability and charge capacity will also be studied. Further optimization of the electrode layer density to improve the specific capacity and the Coulombic efficiency of NIBs is also desirable.

Acknowledgments:

The author would like to appreciate his principal investigator Dr. Brian A. Korgel, mentor Taizhi Jiang, and all the other members of Korgel research group at the University of Texas at Austin. Dr. Marylene Palard and Jean L. Toll helped as the site coordinators. The author would also like to acknowledge the financial support from the National Nanotechnology Infrastructure Networks International Research Experience for Graduates (NNIN iREG) Program and the National Science Foundation (NSF) in the U.S. (under Grant No. ECCS-0335765), and the National Institute for Materials Science (NIMS) in Japan.

References:

- [1] M. D. Slater, et al., *Adv. Funct. Mater.* 23, 947-958 (2013).
- [2] P. R. Abel, et al., *J. Phys. Chem. C* 117, 18885-18890 (2013).
- [3] V. C. Holmberg and B. A. Korgel, *Chem. Mater.* 22, 3698-3703 (2010).
- [4] A. Kohandehghan, et al., *Nano Lett.* 14, 5873-5882 (2014).
- [5] A. M. Chockla, et al., *ACS Appl. Mater. Interfaces* 4, 4658-4664 (2012).

Characterization of Quantum Confined Two-Dimensional Electron Gasses

Veronika Werner

Electrical Engineering, Purdue University

NNIN REU Site: UCSB Nanofabrication Facility, University of California, Santa Barbara, CA

NNIN REU Principal Investigator: Prof. Chris Palmström, Electrical and Computer Engineering, and Materials, UCSB

NNIN REU Mentor: Mihir Pendharkar, Electrical and Computer Engineering, University of California, Santa Barbara

Contact: vwerner@purdue.edu, cpalmstrom@ece.ucsb.edu, mihir@ece.ucsb.edu

Introduction:

Spintronics, or spin electronics, which depend on electron spin, could be faster, smaller and more energy efficient than traditional charge-based electronics. Here, two-dimensional sheets of electrons, or two-dimensional electron gasses (2DEGs), were characterized. They showed properties important to spintronics, such as high electron mobilities and long mean free path. Quantum confined 2DEGs formed in gallium arsenide/aluminum gallium arsenide (GaAs/AlGaAs) heterostructures were simulated using a Poisson/Schrödinger equation solver before the heterostructures were grown by molecular beam epitaxy (MBE). Hall bars were fabricated using photolithography, etching and metal contact formation for use in magnetotransport measurements. The Integer Quantum Hall Effect was observed in these devices and temperature dependence of electron mean free path, mobility and density were studied. These results will be used to develop better material systems for next-generation electronics and spintronics.

Experimental Procedure:

The four basic steps in characterizing two-dimensional electron sheets are design of material structures for quantum confinement, growth of materials, fabrication of Hall bar devices and measurement and analysis.

In the design stage, a Poisson/Schrödinger equation solver [1] was used to simulate the heterostructures. A heterostructure was made up of two or more kinds of dissimilar materials layered on top of one another [2], in this case—materials with different energy band gaps. Gallium arsenide (GaAs) has a relatively low band gap of 1.424 eV at 300 K. Aluminum arsenide (AlAs) has a band gap of 2.12 eV at 300 K [3]. For the heterostructures used here, GaAs was layered with AlGaAs, because the band gap of AlGaAs can be adjusted by changing the Al content.

Two different quantum wells were used, a square well, and an inverted well. The square well had a symmetric layer structure, with gallium arsenide layer in between layers of aluminum gallium arsenide. The inverted quantum well had only one layer of gallium arsenide, with one GaAs/AlGaAs interface, as seen in Figure 1. This differs from a triangular, or conventional quantum well, in that the

low band gap material was at the surface, rather than the higher band gap material.

After a design was chosen, the heterostructure was grown by MBE. Elemental source materials were used and the environment was kept at ultra high vacuum, enabling sharply defined interfaces, sub-monolayer control of thickness, precise control of material composition and minimization of unintentional impurities. This process was essential in achieving the high quality heterostructures necessary for 2DEGs displaying high electron mobility and long mean free path.

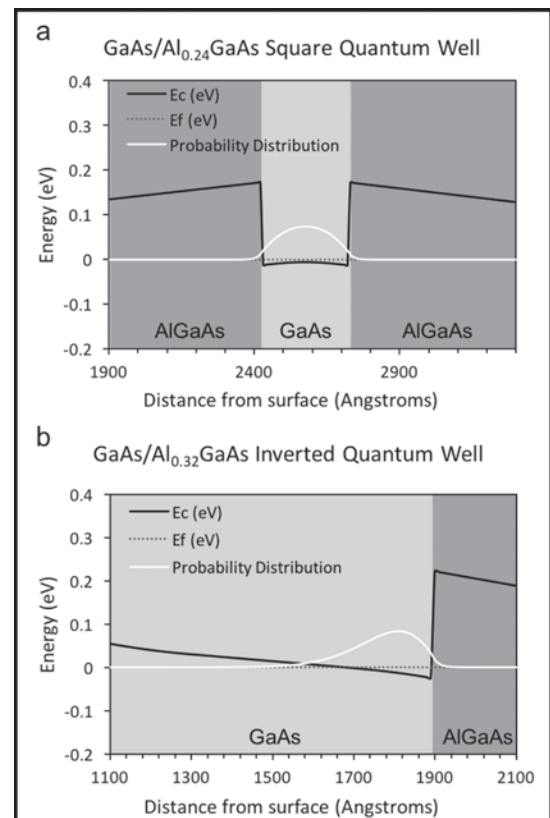


Figure 1: This image shows the conduction bands, Fermi levels and electron waveform probability distribution for; a. a square well, and b. an inverted quantum well.

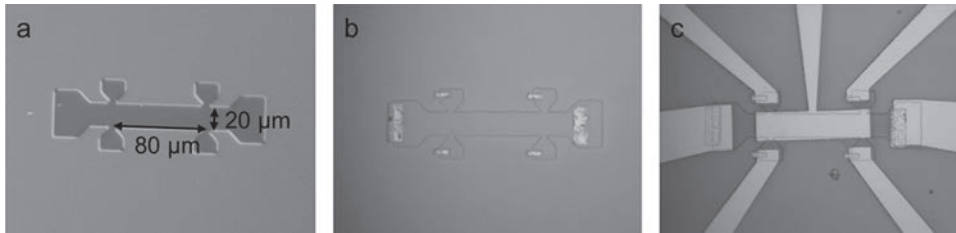


Figure 2: This is a Hall bar; a. after chemical wet etch, b. after metal contact deposition, lift-off and anneal, and c. after metal lead deposition and lift off. Note that the dimensions are $80 \times 20 \mu\text{m}$.

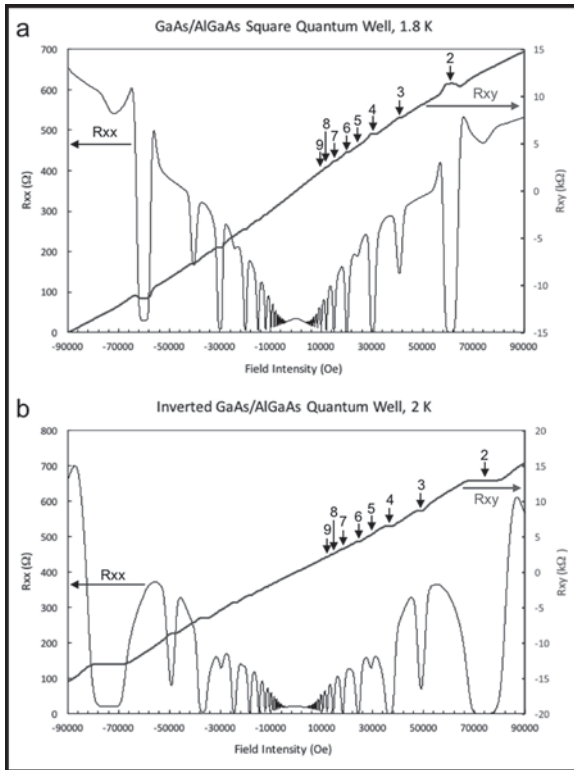


Figure 3: The Integer Quantum Hall Effect observed in; a. a square well, and b. an inverted well. Plateaus in R_{xy} correspond to dips in R_{xx} and occur where R_{xy} is equal to $1/i$ times $h/e^2 \approx 25.813 \text{ k}\Omega$, i being an integer.

Hall bars were fabricated using photolithography. They were simple devices, consisting of a basic rectangle, with connection points for voltage probes and current sources.

Figure 2 shows a Hall bar at various points in fabrication. Figure 2a. shows the pattern after the unnecessary material has been etched away using a chemical wet etch, leaving behind a Hall bar shaped mesa. Figure 2b. shows the device after the deposition of metal contact pads by electron beam deposition and subsequent annealing. The annealing step is necessary to form an ohmic contact, or one that is linear in current/voltage relationship, between the semiconductor and the metal. Finally, metal leads are deposited, as seen in Figure 2c. Their purpose is to connect to the pads and provide a larger surface area to which wires can be bonded.

To determine electron mobility and mean free path, measurements were taken for a range from -9 to 9 Tesla magnetic field and from 1.8 to 300 K for temperature. An alternating current was sourced and lock-in amplifiers were used to measure AC voltages

in order to reduce electrical noise. Two resistances were measured: parallel to current, R_{xx} , and perpendicular to it, R_{xy} , defined as the perpendicular voltage, V_{xy} , divided by longitudinal current, I_{xx} . These values were used to calculate electron mobility, electron sheet density, and mean free path.

Results:

The Integer Quantum Hall Effect, which is a hallmark of 2D electron transport, was observed for the samples tested [4]. Figure 3 shows some of the measured results.

The fact that this effect was observed shows that the structure produced successfully confined the electrons to a two-dimensional sheet. For the two samples whose results are shown, the mobility and mean free path at 2 K for the square well were $870,000 \text{ cm}^2/\text{Vs}$ and $5.48 \mu\text{m}$ and for the inverted quantum well, $1,200,000 \text{ cm}^2/\text{Vs}$ and $7.6 \mu\text{m}$.

Conclusion and Future Work:

These results were typical for the structures that achieved 2DEG confinement, indicating that these samples show promise for future spintronics research. The next steps in this research would be to investigate spin injection into these quantum wells, using ferromagnetic contacts.

Acknowledgements:

I would like to thank my mentor, Mihir Pendharkar, for teaching me about these exciting topics and guiding me through my research. I would also like to thank Prof. Chris Palmström and the rest of his lab group for being so welcoming and sharing their knowledge. This experience was made possible through the NNIN REU Program, and the NSF (under Grant No. ECCS-0335765). The facilities used were part of the Nanofabrication Facility and the Materials Research Laboratory at UCSB.

References:

- [1] Snider, G. 1D Poisson Solver (computer program), UND.
- [2] Kroemer, H. (2000). Quasi-Electric Fields and Band Offsets: Teaching Electrons New Tricks. Nobel Lecture.
- [3] Ioffe Physico-Technical Institute. NSM Archive.
- [4] Störmer, H. L. (1998). The Fractional Quantum Hall Effect. Nobel Lecture.